arXiv:1806.01231v1 [astro-ph.HE] 4 Jun 2018

DIFFUSE X-RAY EMISSION IN THE CYGNUS OB2 ASSOCIATION.

J. F. Albacete Colombo[1], J. J. Drake[2], E. Flaccomio[3], N. J. Wright[4], V. Kashyap[2], M. G. Guarcello[3], K. Briggs[5], J. E. Drew[6], D. M. Fenech[7], G. Micela[3], M. McCollough[2], R. K. Prinja[7], N. Schneider[8], S. Sciortino[3], J. S. Vink[9]

[1] Universidad de Río Negro, Sede Atlántica, Viedma CP8500, Argentina.

[2] Smithsonian Astrophysical Observatory, 60 Garden St., Cambridge, MA 02138, U.S.A

[3] INAF-Osservatorio Astronomico di Palermo, Piazza del Parlamento 1, 90134 Palermo, Italy.

[4] Astrophysics Group, Keele University, Keele, Staffordshire ST5 5BG, UK.

[5] Hamburger Sternwarte, University of Hamburg, Gojenbergsweg 112, 21029, Hamburg, Germany.

[6] School of Physics, Astronomy & Mathematics, University of Hertfordshire, College Lane, Hatfield, Hertfordshire, AL10 9AB, UK.

[7] Department of Physics and Astronomy, University College London, Gower Street, London WC1E 6BT, UK.

[8] I. Physik. Institut, University of Cologne, D-50937 Cologne, Germany.

[9] Armagh Observatory and Planetarium, College Hill, Armagh BT61 9DG, Northern Ireland, UK.

ABSTRACT

We present a large-scale study of diffuse X-ray emission in the nearby massive stellar association Cygnus OB2 as part of the Chandra Cygnus OB2 Legacy Program. We used 40 Chandra X-ray ACIS-I observations covering ~1.0 deg^2. After removing 7924 point-like sources detected in our survey, background-corrected X-ray emission, the adaptive smoothing reveals large-scale diffuse X-ray emission. Diffuse emission was detected in the sub-bands Soft $[0.5:1.2]$ and Medium $[1.2:2.5]$, and marginally in the Hard $[2.5:7.0]$ keV band. From X-ray spectral analysis of stacked spectra we compute a total $[0.5\text{-}7.0$ keV$]$ diffuse X-ray luminosity of $L_x^{\text{diff}} \approx 4.2\times10^{34}$ erg s^{-1}, characterized with plasma temperature components at kT$\approx$ 0.11, 0.40 and 1.18 keV, respectively. The H I absorption column density corresponding to these temperatures has a distribution consistent with $N_H = 0.43, 0.80$ and 1.39×10^{22} cm^{-2}. The extended medium band energy emission likely arises from O-type stellar winds thermalized by wind-wind collisions in the most populated regions of the association, while the soft band emission probably arises from less energetic termination shocks against the surrounding Interstellar-Medium. Super-soft and Soft diffuse emission appears more widely dispersed and intense than the medium band emission. The diffuse X-ray emission is generally spatially coincident with low-extinction regions that we attribute to the ubiquitous influence of powerful stellar winds from massive stars and their interaction with the local Interstellar-Medium. Diffuse X-ray emission is volume-filling, rather than edge-brightened, oppositely to other star-forming regions. We reveal the first observational evidence of X-ray haloes around some evolved massive stars.

Keywords: X-rays: ISM, stars – X-rays: individual (Cygnus OB2) – Stars: massive stars, winds.

1. INTRODUCTION

Since the early X-ray observations by *Einstein* and later *ROSAT*, and up to the last decade, the study of diffuse X-ray emission associated with stellar clusters and star-forming regions has presented considerable challenges. While in supernova remnants or large-scale massive structures, such as galaxy clusters, detections can be quite clear, confirmation of diffuse X-ray emission from Galactic star-forming regions (SFRs) has often remained elusive. Several attempts were made to detect diffuse X-rays from young massive SFRs with ROSAT (e.g., Strickland & Stevens 1998). However, the lack of adequate sensitivity and spatial resolution rendered it difficult to distinguish between genuine diffuse emission and X-ray emission from unresolved stars. Limited by the available instrumentation, this subfield of astrophysics remained without major progress for more than 20 years. This ended in 1999 with the launch of the *Chandra* X-ray Observatory which

combines high sensitivity in the 0.5–8 keV energy range with spectacular spatial resolution ($\approx$ 0.5" on axis). This combination greatly improved the capacity to detect faint X-ray sources and disentangle point source and true diffuse emission contributions in nearby Galactic SFRs. The first genuine discovery of diffuse X-ray emission in a massive star forming region came from the Rosette and Omega Nebulae (Townsley et al. 2003; Muno et al. 2006). Subsequently, *XMM-Newton* observations of the Orion Nebula revealed it to be filled by soft X-ray-emitting (2-MK) plasma (Güdel et al. 2008). More recently, in the context of the "Chandra Carina Complex Project" (CCCP) Townsley et al. (2011a) has published a milestone work for study of X-ray diffuse emission in Carina.

From a theoretical point of view, diffuse X-ray emission is expected to occur in some young stellar associations and SFRs due to supersonic stellar winds from massive stars that can produce dissipative shock waves in the local ISM, modifying astrophysical conditions of the molecular cloud material in

e-mail: albacete.facundo@conicet.gov.ar

the region. These shocks have been interpreted as evidence of non-radiative heating processes (Polcaro et al. 1991) that can give rise to a number of interesting, though poorly explored, high-energy phenomena. However, the processes responsible for the production of X-ray diffuse emission are still not well understood, especially where both thermal and non-thermal (NT) processes may be present. A usual key indicator of thermal diffuse X-ray emission is the presence of spectral lines (Smith et al. 2001), although NT interactions can also produce intense and relatively soft X-ray emission lines ($< 2 \mathrm{keV}$) via the Change Exchange (CXE) mechanism. Otherwise, a featureless spectrum without lines can originate either from thermal processes (e.g., hot bremsstrahlung) or non-thermal electrons via synchrotron emission or inverse Compton (IC) scattering processes.

The first detailed theoretical study was performed in a seminal paper by Weaver et al. (1977). Further development of models for X-ray emission from wind-blown bubbles was carried out by Cantó et al. (2000) and Stevens & Hartwell (2003): they interpreted diffuse X-ray emission associated with massive clusters in terms of a collective cluster wind model (CWM). Winds from individual massive stars with mass loss rates of $\sim 10^{-6}$ $M_\odot$ yr^{-1} and terminal speeds of 1600–2500 km s^{-1} collide, thermalize and expand supersonically into the local ISM. This interaction acts as a precursor of an "interstellar bubble" that expands to a few tenths of a parsec around stars more massive than ~ 8 $M_\odot$. An approximate estimate for a typical single O and/or early B star luminosity and wind kinetic energy is $L_{\mathrm{bol}} \sim 10^{38-39}$ erg s^{-1} and $L_{\mathrm{w}} \sim 10^{36-37}$ ergs s^{-1}. respectively. The adopted typical efficiency of wind momentum to radiative conversion η is 10^{-4} for interstellar shocks (Güdel et al. 2008) resulting in an X-ray diffuse emission luminosity $L_x^{\mathrm{diffuse}} \sim 10^{33-34}$ ergs s^{-1}.

However models of such wind-blown bubbles predict much larger sizes than those reported by Bruhweiler et al. (2010) for the example of the Rosette Nebula. The discrepancy implies that the shocks involved should occur in the radiative (energy loss) regime. Otherwise the high wind speeds should produce strong $\sim$keV X-ray diffuse emission within regions of a few parsec scale. At the same time, evidence for very large "superbubbles" enclosing entire OB associations and shaped by multiple supernovae has been presented. The particular case of the Cygnus superbubble, on a scale well in excess of 100 pc (Cash et al. 1980), is relevant here. But Uyaniker et al. (2001) have argued that the extensive X-ray emission is better viewed as a superposition of a succession of separate regions at different distances. Accordingly, in Cygnus, an investigation of improving high-energy data can make a valuable contribution to clarifying our understanding, and we can access spatial scales of up to tenths of parsec.

In this work, we identify truly diffuse X-ray emission in the Cygnus OB2 association, one of the most massive groups of young stars known in the Galaxy. Assessments of its stellar complement have found that Cygnus OB2 contains well over 100 OB stars (e.g., Schulte 1956; Massey & Thompson 1991; Comerón et al. 2002; Hanson 2003; Wright et al. 2015b) and tens of thousands of lower-mass, pre-main sequence stars (e.g., Albacete Colombo et al.

2007; Drew et al. 2008; Vink et al. 2008; Wright & Drake 2009). Cygnus OB2 lies at the center of the Cygnus X giant molecular cloud and star forming complex (Schneider et al. 2006; Reipurth & Schneider 2008), and is a source of feedback for the region (Wright et al. 2012; Guarcello et al. 2016). Its size and proximity make Cygnus OB2 an ideal environment to search for diffuse emission resulting from feedback into the environment from massive stars.

This study forms a part of the science exploitation of the *Chandra* Cygnus OB2 Legacy Survey (Drake et. al., this issue). This 1.1 Ms survey comprises a mosaic of *Chandra* ACIS-I pointings covering the central square degree of the association, which contains the majority of the massive young stellar association. The observations and the source catalog are described in Wright et al. (2014a). Guarcello et al. (2017) have matched X-ray sources with available optical and infrared (IR) photometric catalogs, while Kashyap et al. (2017) have applied statistical methods to separate out approximately $\sim$6000 sources identified as association members from an additional ~ 2000 sources assessed as foreground and background interlopers. Flaccomio et. al. (2018) characterize the X-ray spectral properties of these populations, and discuss the results in the context of different emission models. This thorough assessment of the point source content, combined with the deep and wide nature of the *Chandra* survey itself, provides a valuable dataset for a thorough exploration of X-rays from diffuse gas in the region.

In this article we focus on the analysis, detection and morphological description of diffuse X-ray emission in Cygnus OB2. We discuss its origin and derive approximate astrophysical properties of the diffuse X-ray structures at large and small scales.

2. X-RAY OBSERVATIONS AND DIFFUSE EMISSION ANALYSIS

The study of the diffuse X-ray emission is of interest for assessing the total X-ray output of a region like Cygnus OB2, and will be important for understanding the X-ray emission from much more distant, unresolved stellar clusters. The expected diffuse X-ray emission from Cyg OB2 will be spread over a large angular sky area (~ 1 sq. deg.) and will have a correspondingly low surface brightness. An interesting rough comparison is the expected diffuse signal compared with the combined signal from detected point sources. We can estimate the X-ray luminosity of the detected Cygnus OB2 stellar population by assuming that: *i*) we detect all members with mass $> 1 M_\odot$ (Wright et al. 2015a) *ii*) the IMF of Cygnus OB2 is similar to that of the Orion Nebular Cluster (ONC), and *iii*) Cygnus OB2 stars have the same X-ray activity as derived for ONC stars by Preibisch et al. (2005). Adopting the "lightly absorbed optical sample" as representative of the low-mass ONC population, we estimate that the Cygnus OB2 population of stars with mass between 1.0 and 10 $M_\odot$ is $\sim$10 times larger than the ONC one. We can then scale the total luminosity of the ONC sample by this factor, obtaining $L_x^{\mathrm{LMS\ total}} \sim 2 \times 10^{34}$ erg s^{-1} for the whole association, which is comparable to what we expect for the diffuse emission. To
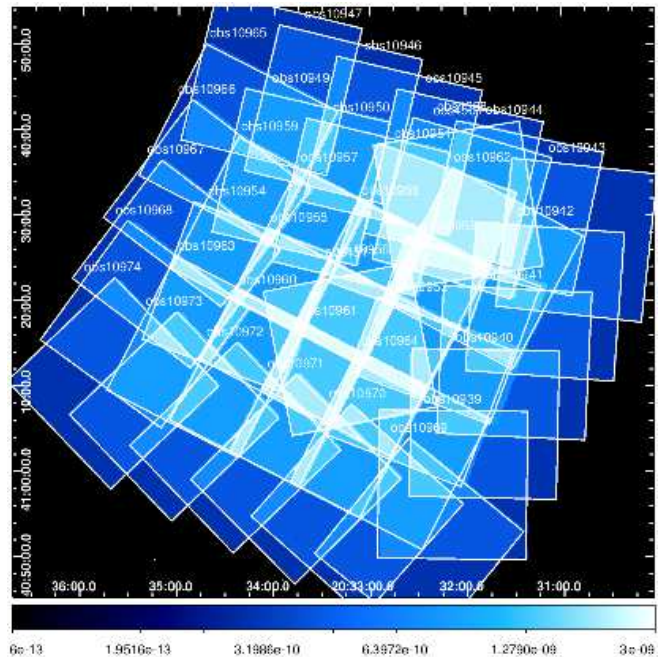
deal successfully with the difficult task of extracting the diffuse emission signal, we made use of the specific data analysis software ACIS-Extract (AE) (Broos et al. 2012), which is able to remove the point source X-ray emission via the construction of "swiss-cheese" ACIS-I images with holes at the positions of detected point sources. It computes the local point spread function (PSF) at each source position and masks its local contribution to the observation (see section 2). However, the removal of all detected point sources does not of course guarantee that the remaining X-ray emission will be truly diffuse, since the summed contribution of undetected faint sources could masquerade as diffuse X-ray emission. To assess how big this problem is, we adopt the completeness limit of the survey in the central 0.5 sq.deg as computed by Wright et al. (2015a). Assuming that the distribution of X-ray luminosities at a given mass is the same as in the ONC, as sampled by the Chandra Orion Ultradeep Project (COUP) "lightly absorbed optical sample", and that the population is 10 times as large (see above), we estimate that the X-ray luminosity of the undetected population of sources is $\sim 4.5 \times 10^{33} \mathrm{erg\,s^{-1}}$.

2.1. *Data reduction and processing*

We made use of the set of 37 X-ray pointings of the *Chandra* ACIS-I camera that were acquired in the context of the *Chandra* Cygnus OB2 Legacy Program (Drake et al., this issue). An additional set of three existing observations were included within the survey area, which had previously been used to study the Cyg OB2 association (Butt et al. 2006; Albacete Colombo et al. 2007; Wright & Drake 2009). The total of 40 pointings were acquired in the VFAINT (5x5 pixel island) mode, which is an optimal choice for identifying and removing events that originate from the end-points of particle event tracks and that cannot be removed using a standard grade analysis based on 3x3 islands[1]. This observational setup is crucial to disentangling true X-ray diffuse emission photons from instrumental and background effects. The survey was performed over a central 0.5 deg^2 of the Cygnus OB2 association with an effective exposure of 120 ksec and an outer 0.35 deg^2 area with an exposure of 60 ksec. The description of the survey design and observations, the data reduction and source detection, has been presented extensively in Wright et al. (2014a).

All 40 ObsIDs were uniformly reprocessed using version 4.8 of the CIAO software (Fruscione 2014), combined with CALDB 4.7.1 calibration database files. In order to get consistency in the calibration procedure, we re-ran the Level 1 to Level 2 processing of event files using the CIAO CHANDRA_REPRO meta task. The CHECK_VF_PHA=YES option was set to flag bad events and then filter them. The new Level 2 event file was produced by filtering events to status==b0. The initial set of observation were processed with older *gain* files and were updated during the ACIS_PROCESS_EVENT to the lastest available file version. Similar treatment was applied to the background event files (see section 2.1 for details). Since the available "stowed" background files (from which the energetic particle event background can be estimated) were made

using only quiescent background periods, background flares needed to be excluded from our observations in the exactly same way for consistency. We extracted light-curves with the same time bin size as was performed for the background files (bin=259.28 sec), and we made use of the DEFLARE CIAO 4.8 Python routine[2]. We time-filtered all of the observations. The time reduction was found to be necessary, and in the worst case this amounted to less than 4% of the total exposure of an observation. In order to avoid intense instrumental emission lines (see section 2.2), we filtered the whole set of observations to exclude all events outside of the 0.5-7.0 keV energy range.

Figure 1. The exposure map for the Cygnus OB2 Chandra Legacy Survey and complementary observations for the study of diffuse X-ray emission. The bottom color bar shows the flux to color normalization factor in erg cm^{-2} s^{-1}.

The reprocessed event files and this set of observations are essentially the starting point of our analysis. We computed monochromatic exposure maps for all 40 X-ray observations using the AE_MAKE_EMAP AE task for representative photon energies of 0.7, 1.7, and 3.5 keV. In Figure 1, we show the mosaic of exposures at 1.7 keV of all the observations used in the Cyg OB2 survey. We use each of these sets of images to normalize the count images in different energy bands of [0.5–1.2], [1.2–2.5] and [2.5–7.0] keV, respectively, to produce X-ray fluxed images uncorrected for interstellar absorption. However, as the diffuse X-ray emission is faint, the confirmation of its existence depends on careful analysis of the background (sub-section 2.2), as well as a thorough assessment of the contribution from X-ray point sources (sub-section 2.3).

2.2. *Background analysis*

---

[1] See further details in http://cxc.harvard.edu/Acis/Cal_prods/vfbkgrnd/

[2] See http://cxc.harvard.edu/ciao/ahelp/deflare.html

Analysis of faint extended X-ray diffuse emission is an inherently difficult task, as the emission is spread over the detector and is affected by non-local background such as solar and radiation belt energetic particle events, and X-ray events from interloping sources such as active galactic nuclei (AGNs). As noted above, the instrumental and energetic particle background was assessed using a set of ACIS stowed observation files[3]. Since the ACIS instrumental background is known to be time-varying, the proper scaling of these images to a given observation cannot be estimated from relative exposure times alone (see, e.g., details in Section 4.1.3 of Hickox & Markevitch 2006). Thus, background images were also scaled to match the spectra of each of the 40 observations in the 7–12 keV range, where the stellar emission has no significant signal (see Figure 2).
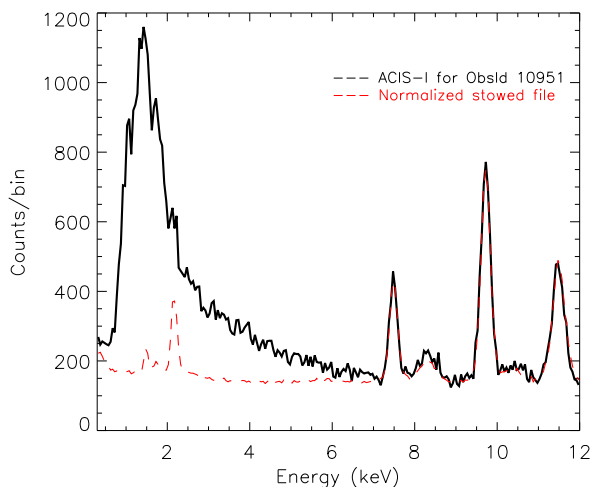
Figure 2. Pulse height distribution of events for ObsId 10951 (black continuous line) together with the stowed background normalized to match based on fluxes at energies of 7.47, 9.8 and 11 keV, where the sky has no emission (red dashed line). The weaker ~ 2.1 keV emission line is also instrumental, but was not used to match stowed-observation events and so it could be present in some diffuse X-ray spectra.

Finally, we constructed new stowed exposure maps for the next step of the analysis, which uses mask stowed event files and new stowed exposure maps for use at each source position.

2.3. *Masking X-ray point sources*

Here we give details of the procedure implemented to reduce the impact of X-ray point sources on the event and calibration (stowed) data files. We used the specific task AE_MASK_STOWED_DATA from the AE code that masked event files, exposure maps, and both stowed events and stowed exposure files. We thus subtracted events from a total of 7924 X-ray point sources listed in our catalogue (Wright et al. 2014a) covering all 40 of the ACIS-I observations.

The first step in the point source subtraction is to build intensity models for sources, as well as for readout streaks,

and draw masks around them to compute an image that models the signal from all these features. We use the task AE_BETTER_MASKING from AE to adaptively compute source emission at the 99% enclosed energy aperture threshold. Such a mask fraction is more than adequate for faint sources with only a handful of counts, since the probability of losing genuine source events in the PSF wings is low. In cases where the X-ray source was intense, the source wings were inspected close to the masked event data to see if there were remaining wings from scattering photons that are bright enough to locally contaminate our diffuse emission analysis. In such cases, we arbitrarily increased the mask size by multiplying up to a factor 1.5 times the 99% PSF limit (Townsley et al. 2011a). Under this condition, the AE recipes assure that source event photons in the wings of the PSF, or photons scattered out of the PSF, should fall below the local background level of the observation (Broos et al. 2012). In Figure 3-left, we show the resulting source + readout streak emission models. Otherwise, the Figure 3-right show the residual map of the cropped sources, that consist in the difference between the observed source count image and the source+streak intensity models (left-image). Hereafter we refer to these residual images as "wings" files. Note that the wings image peaks at the log(Source wings)≈-1.45. It means, that the maximum "wings" contribution to the observed emission image is only about 3.5%, or less. Both maps shown correspond to obsID 10951, that hereafter will be used to illustrate the analysis that was applied to the rest of the observations.

3. ADAPTIVE SMOOTHING STRATEGY

One of the most critical issues in the study of X-ray diffuse emission is the choice of smoothing strategy. For this purpose, we made use of the TARA_SMOOTH tasks[4]. We used the top hat adaptive kernel smoothing. All maps were computed in a 512×512 array. Larger 1024×1024 maps did not produce better results and were also computationally very demanding. Two main parameters that play a major role in smoothing are the i) significance, which is a scalar or vector number specifying the desired Signal-to-Noise (S/N) ratio of the smoothed flux image, and ii) the smoothing radii that could be imposed to achieve the same spatial smoothing scales in different energy bands. The radii of smoothing are limited to a maximum of 71 pixels, and the imposed S/N condition is only applied if smoothing radii remain below this limit. The smoothing procedure was initially run for the full [0.5–7.0] keV band. After several runs at S/N ratios of 9, 12, 16, and 25, we found that S/N~16 is the best compromise between the imposed S/N condition, smoothing radii, and the ability to unveil true X-ray diffuse structures at spatial scales greater than the smoothing radii all over the field of view (see Figure 4). The units of the resulting flux maps are ph/cm^2/s/arcsec^2.

For sub-band images in the energy ranges in keV Soft [0.5–1.2], Medium [1.2–2.5], Hard [2.5–7.0] and total [0.5–7.0], we adopted a different smoothing strategy. We decided to
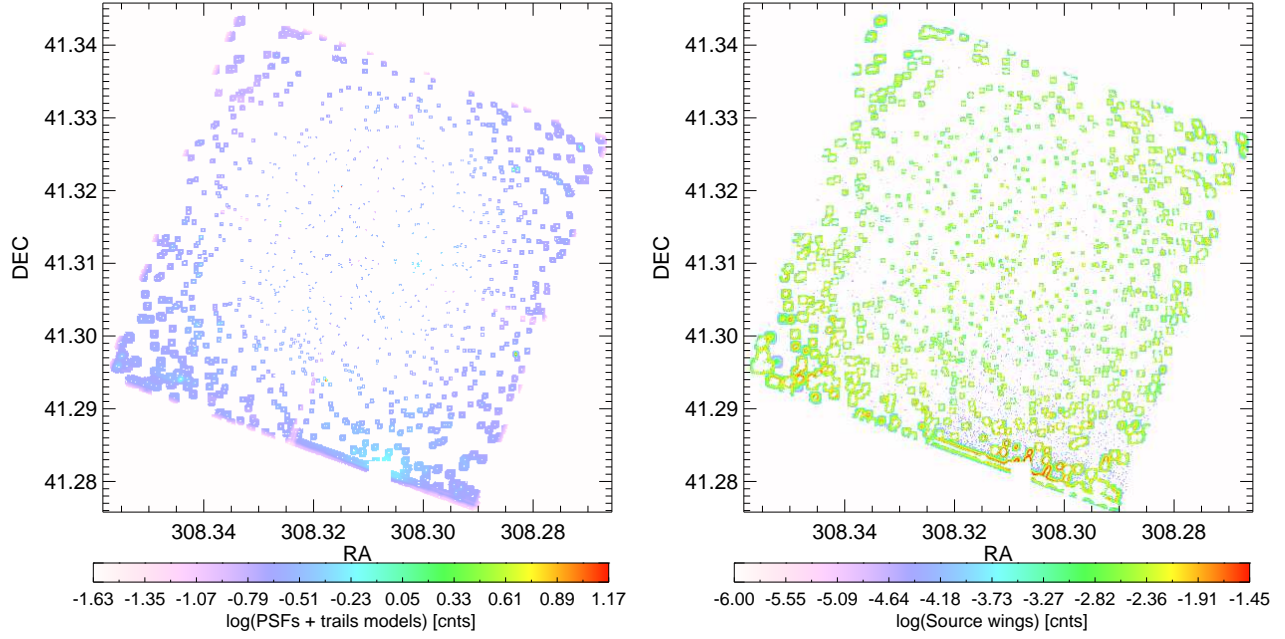
Figure 3. ObsId 10951, illustrating the treatment of point sources and their exclusion from diffuse emission maps. Same analysis were applied to the whole set of observations. Left: Show the source PSF and readout streak intensity models that were computed on the list of detected sources in the observation. Right: Show the residual PSF wings image which was computed as the difference between the observed source count image and the source+streak intensity models (left-image). Scale bars of both panels show the intensity range in which the images spans.
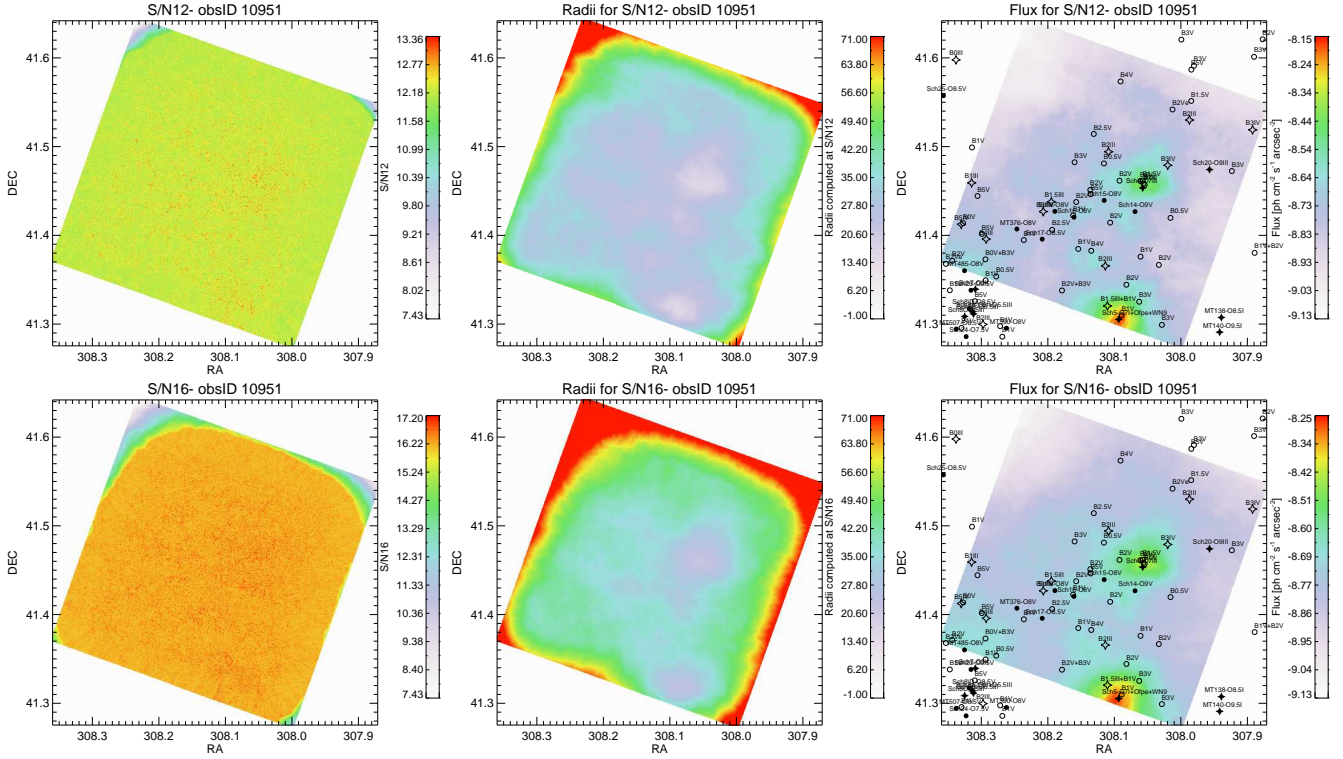
Figure 4. Exemplification of the procedure for the ObsId 10951. Left panels: the S/N significance map computed at the imposed condition of S/N=12 and 16 respectively. Central panels: The tophat radius computed to reach the imposed S/N condition. Up to the borders of the observation, the tophat radii increase as much as necessary to achieve the S/N, although once off the detector the signal falls to zero and can reduce the final S/N below the desired threshold. Right panels: X-ray diffuse emission flux [ph/cm^2/s/arcsec^2] in the [0.5–7.0] keV energy range computed at S/N~12 and 16, respectively. Note that the peak of emission changes slightly for different S/N owing to the different binning, but by just 0.1 dex or roughly 25%. At the limit of detection of the diffuse emission of log(F_x)≈-8.64 or -8.69, for S/N=12 or 16 respectively, the difference is only 0.05 dex, or about 11%. Black filled star symbols indicate the evolved massive stars with conspicuous X-ray emission; open star symbols refer to evolved massive stars without X-ray emission; black filled and empty circles indicate main sequence massive stars, with and without detected X-ray emission, respectively. The list of massive stars in Cygnus OB2 was taken from Wright et al. (2015b).

smooth sub-images using the same set of radius kernels com-   puted to achieve a given S/N ratio in the band with poorest
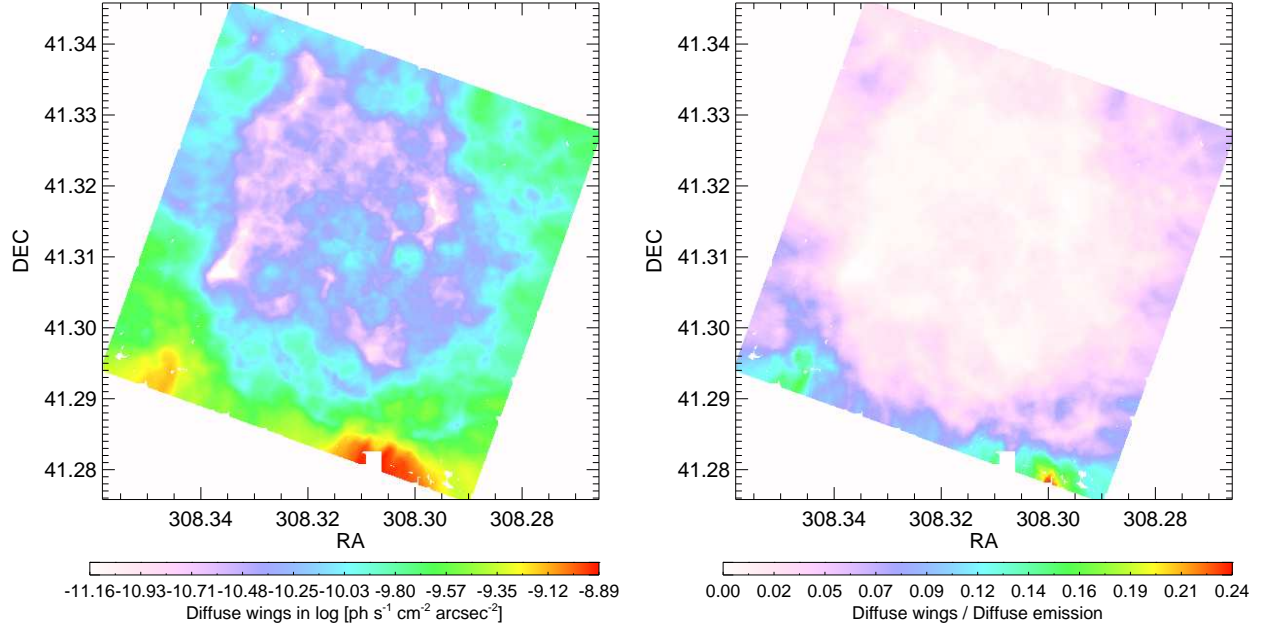
Figure 5. Exemplification of the procedure for the ObsId 10951. Left: Source wing diffuse contribution in the [0.5-7.0] keV energy range computed using fixed smoothing radii for S/N≥ 16 in the full band. Right: the ratio of wings to total diffuse emission has a maximum contribution of 0.24, which lies at the border of the map. The median contribution from wings all over the image is about 6%.

photon statistics. We adopted S/N~16 to avoid smoothing radii becoming too large, with this condition relaxed at the borders of the detector. For the rest of the bands, smoothing was performed by fixing the smoothing radii map to that of the Soft band via the optional parameter FIXED_RADIUS_MAP_FN. As the Medium and Hard X-ray bands have better photon statistics, the significance of such maps reach higher S/N than in the soft band. In this way, we guarantee that the adopted S/N ratio is always achieved for the rest of the energy band maps, as well as ensuring that the spatial scales of the maps are adequate for construction of hardness ratio maps.

3.1. *The X-ray source wing diffuse contribution*

Based on the smoothing considerations presented in Section 3, we are able to estimate the contribution to diffuse emission produced by photon events in the extreme wings of sources that were not adequately excluded by the computed masked regions. To do this we applied the same smoothing constraints used for the diffuse maps to the source wing diffuse maps of Figure 3 (right). The TARA_SMOOTH routine was fixed to radii computed for the flux diffuse emission at S/N≥ 16.

In Figure 5 (left) we show the resulting diffuse wing emission contribution for ObsID 10951. The emission peaks at $\log(f_x) = -8.89$ ph/cm^2/s/arcsec^2, at large off-axis angles as a consequence of ill-constrained source + readout streak emission models related to the intense diffuse X-ray stellar source Schulte #5 (see section 3.1). In order to quantify such possible contributions over the entire set of the observations, we computed the diffuse wings/total emission (f_{wings} / $f_{diffuse}$) maps to identify possible spatially-resolved wing contamination zones. In the right panel of Figure 5, we can assert that, except for the very edges of the observation field of view, diffuse wing source contamination remains, in media, under 6% over the FOV.
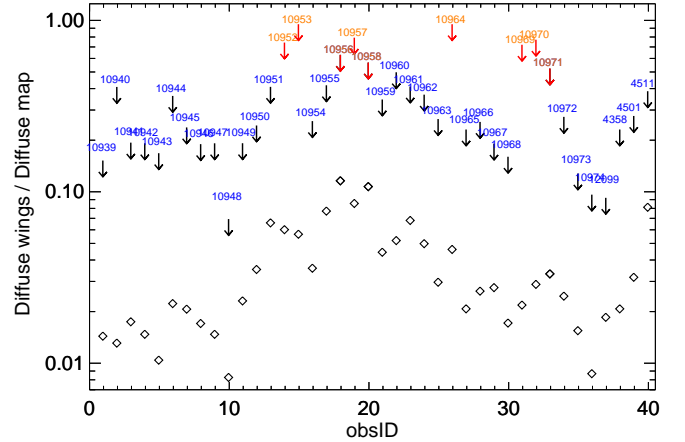

Figure 6. Down arrows indicate maximum contributions of source wings to diffuse emission (see text for details). Red arrows indicate observations that are likely to be affected by gas and dust scattering processes related to the intense emission from Cygnus X-3. Black diamonds correspond to the median of the wings to diffuse emission ratio for the entire FOV of each observation.

Next, we computed the median ratio of the f_{wings} / $f_{diffuse}$ contamination for each of our observations. In media, these values illustrated in Figure 6, range between 1 and 10 %. However, there are some regions in which the ratio f_{wings} / $f_{diffuse}$ peaks at over 50% (ObsIds 10952, 10953, 10956, 10957, 10958, 10964, 10969, 10970 and 10971). This occurs only for some intense sources located at large off-axis angles, or at the chip borders of the observations because of read out streak events or because the source PSF itself cannot accurately modelled. These high ratios do not inconvenience our diffuse analysis at all, as they correspond to very small fractions (typically ≤ 4 to 6 %) of the map areas. We avoided

these parts of observations in the diffuse X-ray analysis, and instead used observations in which the same sky region appears close to on axis, where the masked model describes adequately the local PSF of the sources.

4. X-RAY HARDNESS RATIO MAPS

The construction of X-ray hardness ratio (HR) maps is a useful method of getting a first order approximation of the spatial energy distribution of X-ray photons without losing spatial resolution. We produced [count-rate] maps in (S)oft [0.5–2.5 keV] (S) and (H)ard [2.5–7.0 keV] X-ray bands, and computed HR as the ratio of the difference to the sum, i.e. (S-H) / (S+H). In this way we are able to discern soft and/or hard features in the diffuse X-rays regardless of their relative intensity. All HR maps were computed from maps that were smoothed using the tophat method, but considering the fixed smoothing radius computed for a signal-to-noise ≥16 in the soft band (see S 3 for a full explanation). We thus avoid false diffuse structures that would appear due to differences in the radii of the maps. HR maps were constructed for the entire set of observations in the survey (see Appendix).
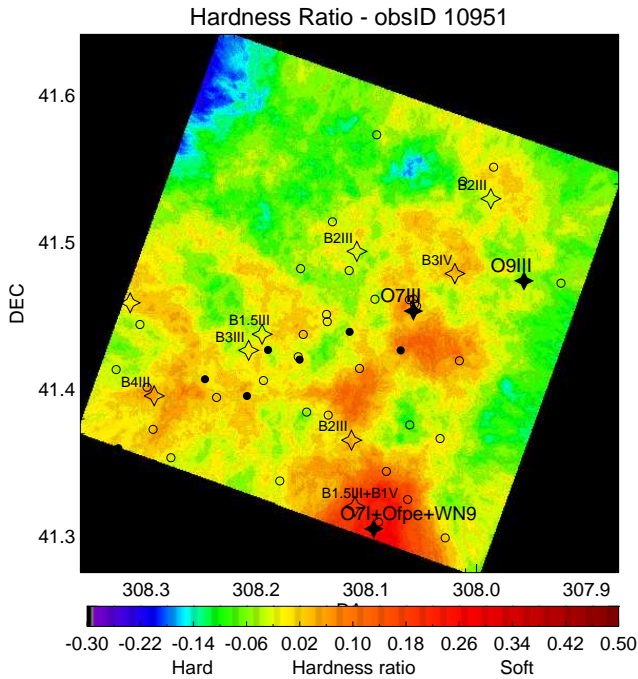
ergetics of the diffuse X-ray emission, providing clues about the impact of massive star stellar winds on the spectral energy distribution of the diffuse X-ray gas, even in those regions bereft of bright X-ray sources or with high ISM density.

The natural explanation for what we are seeing is that evolved massive stars in the region fill the volume of space between the massive stars with the summed contribution of hot shocked stellar winds. Eventually, these encounters drive a slow shock into the ISM, that contributes to the excitation of the observed H_α emission and, via the presence of dense neutral gas and/or dust structures absorbs and re-emits radiation in X-rays (see section 7 for discussion).

However, not all HR values in the maps are descriptive of the energy of diffuse X-ray emission from shocked gas, and in those places where the diffuse emission is undetected, or absent, the extragalactic X-ray background also appears to play a role in some cases (see sub-section 4.1).
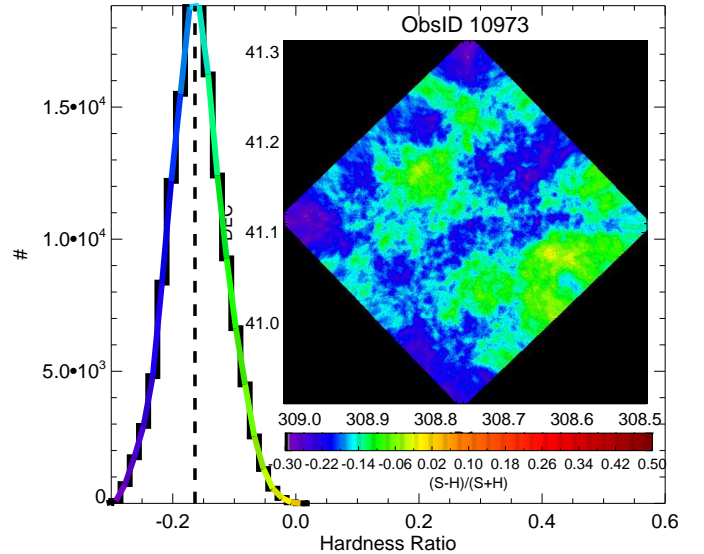
4.1. *Hardness ratio of the background*

Figure 8. Hardness ratio histogram for ObsID 10973. No obvious Cygnus OB2 X-ray diffuse emission was seen in this observation (see middle panel-right of figure 27 in Appendix), so that the observed HR corresponds to that of the background emission. Colors in the histogram corresponds to those of the color bar of the image. The peak of the HR distribution is about -0.16 for a 1σ of 0.06.

Figure 7. Exemplification of the HR analysis for the ObsId 10951. The scale color bars show the range in HR that the image spans. Black filled and opened star symbols indicate the evolved massive stars with and without intrinsic X-ray emission, respectively (from Wright et al. (2015b)). Filled and open circles indicate MS massive stars, with and without intrinsic X-ray emission, respectively. Note that the diffuse gas follows the spatial distribution of the massive stellar population, regardless of whether they are strong X-ray emitters. The entire set of HR maps is shown in the Appendix.

A serious difficulty in characterizing the diffuse emission energy distribution using HR maps concerns the problem of where the background becomes dominant, and how to estimate a typical HR value for it. We make an initial estimation by searching for X-ray observations (or places in Cygnus OB2) in which X-ray diffuse emission appears to be absent (e.g. ObsID 10973 in Figure 26 of the Appendix). In this observation, no massive stars are in the FOV, and it is also unaffected by background scattering of X-rays from Cygnus X-3.

Figure 7 shows that softer diffuse emission follows the spatial distribution of massive stars from Wright et al. (2015b), even in those cases where massive stars do not emit significant X-rays themselves. As we discuss further below, the sensitivity of the HR maps highlights small changes in the en-

We computed the HR energy distribution of the smoothed background for the entire field of view of obsID 10973, finding it peaks at -0.16±0.06. We have simulated a set of power-law emission spectra that adaptively constrains the observed

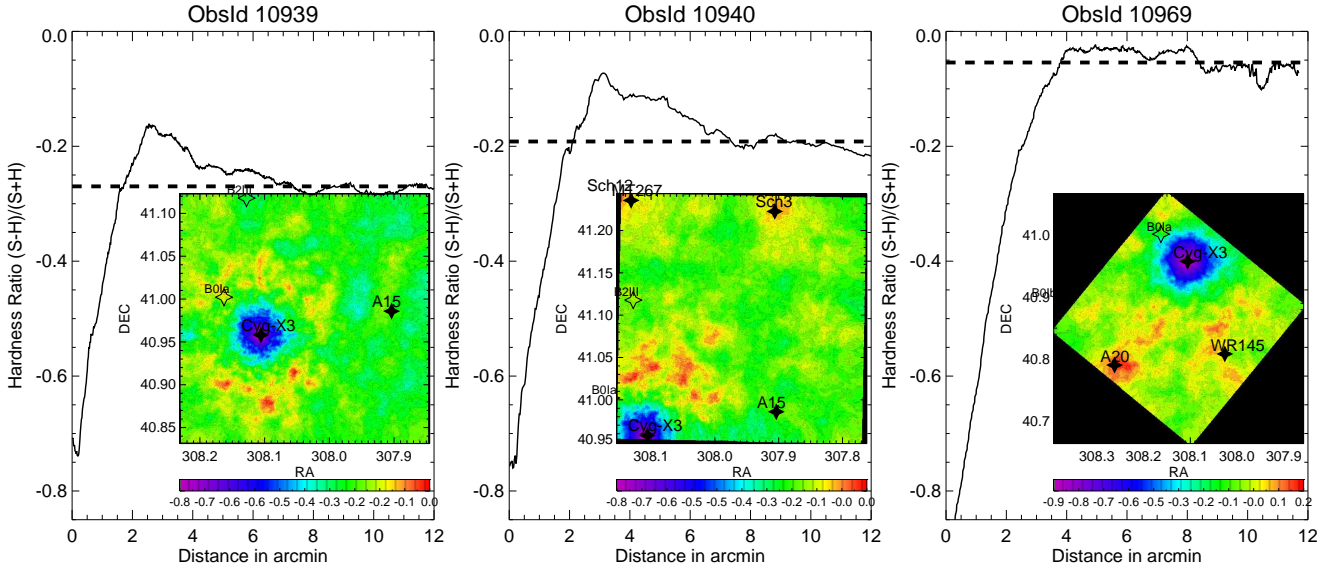**Figure 9.** Cyg X-3 HR radial profiles of HR maps. Diffuse scattering extends to typical HR ≈ -0.14±0.07, where in worst of case, it drops to the level of the ambient Cyg OB2 HR at a radial angular scale of ≈ 8 arcmin. Beyond this range we consider the influence of Cygnus X-3 scattering on the diffuse X-ray emission to be negligible.

HR values on this map. Typical Γ indexes range from 1.0 to 1.3, which agree with the expected spectral index for Active Galactic Nuclei (AGN). In fact, this estimate of the hard X-ray background is known as the "X-ray Background Hardness Problem" and originates from obscured AGN, as discussed by May & Keel (2008). This problem refers to the cumulative contribution to the background of hard (energy ≥ 3 keV) emission from discrete unresolved sources (AGN), each one emitting below the detection threshold of the observation. More precisely, for the total of ~ 1450 background X-ray sources in the Cygnus OB2 survey (Kashyap et al., this issue), we found the extragalactic contribution consistent with an N_H absorption ≈ 2.0(±0.09)×10^{22} cm^{-2}, and a power law Γ index of 1.3(±0.05) (Flaccomio et al. this issue), which agree with typical HR ≤ -0.1 values for AGN.

In summary, hard unresolved AGN do not play a major role in the typical HR of the local diffuse emission, and its hard contribution appears homogeneous across the field of the observation (see HR map of the obsID 10973). This last conclusion agrees with the detailed analysis of the absorption along the line of sight of this region, that was independently computed and extensively discussed for the foreground, member and extragalactic X-ray source populations (Flaccomio et al., this issue).

4.2. Dust scattering from Cyg X-3 emission

Cygnus X-3 is known to be a γ-ray source located in the background at a distance of 7.4 ±1.1 kpc (McCollough et al. 2016), more than five times farther away than the Cygnus OB2 stellar association itself. Its radiation in X-rays is essentially hard (≥ 3.5 keV; Koljonen et al. 2010), although in the soft (0.5-2.0 keV) X-ray band it is intense enough that it could mask any prominent diffuse structure in the vicinity of the line of sight, even when the source PSF has been masked at radii 1.5 times larger than the 99% Encircled Energy Fraction (EEF). We have attempted to mitigate the influence of Cyg X-

3 by disentangling hard and soft X-ray emission through the HR coded image, allowing us to reduce the impact of scattered photons as well as to explore how far the scattering extends.

In six of the 40 X-ray observations of the survey, the scattering halo around Cyg X-3 was observed, either totally or partially, namely in ObsIds 10939, 10940, 10964, 10969, 10970 and 12099. In Figure 9 we show the HR radial profiles and the smoothed images. As scattered radiation is dominated by hard photons, even harder than expected from the unresolved AGN background radiation, the peak of the HR reaches very negative values at the centre, with HR≈ -0.8. However, as the intensity decays with the inverse square of the radial distance (r^{-2}), at larger distances the influence of scattered X-ray photons from Cyg X-3 decreases to the typical HR of the background (HR_{bkg}). At such a distance the radial profile becomes flat. On average, for all the observations we estimated that the HR_{bkg} levels off at large radial distances from Cyg X-3 at -0.14±0.07, which is consistent with the value obtained in Section 4. The typical scattering halo of Cyg X-3 extends to a radius of about ~ 8 arcmin.

We note the existence of some softer sub-structures (HR ≥ 0.05) surrounding Cyg X-3, which are probably due to scattering from dust clouds along the line-of-sight to Cygnus X-3 (McCollough et al. 2013). Otherwise, HR values below −0.1 cannot realistically be considered part of the diffuse X-ray emission, as temperatures are required to be above 7 keV, which is unconstrained for the limited energy range of the observation. In any case, besides the poor photon statistics in such bands, HR values of ≈ −0.1, or harder, would be better described by a simple power-law emission model with spectral index Γ = 1.7 or lower (Corral et al. 2011). Hereafter, conservatively, reliable diffuse X-ray emission patterns in the HR maps would be considered for those HR values larger than ≈ −0.1.

5. LARGE-SCALE DIFFUSE X-RAY MAP

The morphology and energetic large-scale appearance of diffuse X-ray emission in the Cygnus OB2 association is shown in Figure 10-left. It is a mosaicked, point source-removed image in the [0.5-7.0] keV energy range. Similar images were also made in three discrete energy bands: Soft [0.5-1.2] keV, Medium [1.2-2.5] keV and Hard [2.5-7.0] keV. These images include the complete set of ACIS-I observations of our survey and cover an area of about 1 deg^2 (see Section 7).

Mosaicking was performed using the Montage software to generate a list of images with corresponding WCS information. Before reprojection, we computed the individual emission levels required to match overlapping images. To do this, we determined the average emission level of two or multiple overlapped observations and scaled each image to match this average emission level. In cases of multiple overlapped images, the average diffuse emission level was computed by equal weighting averages. While more complex overlapping functions (e.g., cubic splines) might be employed, and can in principle work well to match background levels in overlapping observations with X-ray point sources, we found that spline smoothing functions at the faint X-ray diffuse emission levels that characterize the Cygnus OB2 observations can be numerically ill-conditioned, producing biased spline coefficients, not only resulting in mismatched scaling at the borders of each observation, but also producing fake large scale structures.

In the process of obtaining a full coverage diffuse X-ray emission map for the observed Cygnus OB2 region, and accounting for all the issues that could affect the diffuse X-ray emission level, we still need to account for one other possible underlying contamination problem, which is the contribution from the unresolved population of low mass stars, in the stellar mass regime in which our survey detection is incomplete.

5.1. Unresolved stellar population vs. diffuse X-ray emission

One of the major problems facing the detection of diffuse X-ray emission in SFRs is the underlying contribution from unresolved sources that individually give rise to counts that fall below the detection threshold of the region. Three different contributions are addressed separately:

i- *Background contribution:*
Guarcello et al. and Wright et al. (this issue) found that about 78 % (6149 / 7924) of X-ray sources detected in the *Chandra* survey were classified as Cygnus OB2 members. For background objects (1304 sources classified), the contribution from undetected AGNs remains under the detection threshold all over the entire set of observations, as was computed at the centre of our Cygnus OB2 region using a deeper (100 ksec) observation (Albacete Colombo et al. 2007).

ii- *Foreground contribution:*
The case of undetected foreground stars is more controversial, because they appears softer than that of the background sources (see Flaccomio et al., this issue), and so it is expected to be more difficult to distinguish from the spectrum of the diffuse emission. Based on the classification analysis of Chandra X-ray sources in the Cygnus OB2 region, we have identified ~471 X-ray sources (~6% of the total) as foreground stars (Kashyap et al., this issue). The stacked spectrum of all individually-detected foreground stars towards the Cygnus OB2 region shows a soft thermal plasma emission with typical temperature and absorption of kT = 0.77 keV and $N_H^{upper\ limit} \approx 0.2 \times 10^{22}$ cm^{-2}, respectively (see Flaccomio et al., this issue). The total unresolved foreground stars are likely to have a similar spectral shape that could easily contribute to the observed soft diffuse X-ray emission. However, the clear anti-correlation between diffuse X-ray emission and observed colder gas-dust structures in the Cygnus OB2 association (see discussion in Section 7), suggests that the soft diffuse emission we detected is mainly associated to the Cygnus OB2 region. Alternatively, we used the investigation of Getman et al. (2011) that estimates the star foreground unresolved population of 200,000 toward Carina (2.3 kpc and Area~ 1.42 sq.deg.). By scaling to the Cygnus OB2 region (1.4 kpc and Area ~ 0.97 sq.deg.) we estimate ~ 18,500 unresolved foreground stars that would be in the projected area of the survey. They would emit at levels below the typical detection threshold of the survey of 6×10^{-5} cnts/s (~ 3 photons) (Wright et al. 2015a). So, the total number of expected photons from unresolved foreground stars is less than or equal to $3 \times 18,500 \approx 56,000$ photons, or just ~ 8% of the total of counts (~ 710,000) observed in the entire 0.97 sq.deg Cygnus OB2 diffuse X-ray emission map.

iii- *Stellar Cygnus OB2 contribution:*
In order to compute the contribution to the observed X-ray diffuse emission level from unresolved low-mass stars belonging to the Cygnus OB2 region, we adopted the completeness limit for the survey from Wright et al. (2014b). With some small spatial variations (generally 10% or less in terms of flux), the X-ray luminosity completeness limit for our Cygnus OB2 survey area ranges from 50% at 1.4×10^{30} ergs s^{-1} to 90% at 4×10^{30} ergs s^{-1}. The actual percentage of stars detected is different for stars of different masses because the X-ray luminosity distribution is mass-dependent. For the entire survey area the completeness is 50% at 0.6 M$_\odot$ and 90% at 1.3 M$_\odot$, respectively (Wright et al. 2014b). For our purposes, the X-ray luminosities of stars were computed by adopting the X-ray conversion factor (CF), i.e. the ratio between unabsorbed flux (f_{ua}) in ergs to the absorbed flux in photons (f_{abs} [ph]), that corresponds to a value of 5.4×10^{-9} [erg/ph] (see Flaccomio et al, this issue).

We assumed the X-ray luminosities of the stellar population of Cygnus OB2 stars at masses in which our survey is essentially complete are the same as stars of the same mass in the Orion Nebular Cluster (ONC). We then used the results of the Chandra Orion Ultradeep Project (COUP), that is essentially complete at all masses above 0.3 M$_\odot$ (Feigelson et al. 2005; Getman et al. 2005; Preibisch et al. 2005), to infer the signal from stars in Cygnus OB2 with masses below 1.0 M$_\odot$ for which we are complete to a level of about 85%.

The expected X-ray luminosity contribution for stars with masses in the range [0.3 − 1.0] M$_\odot$, per star in the ONC is
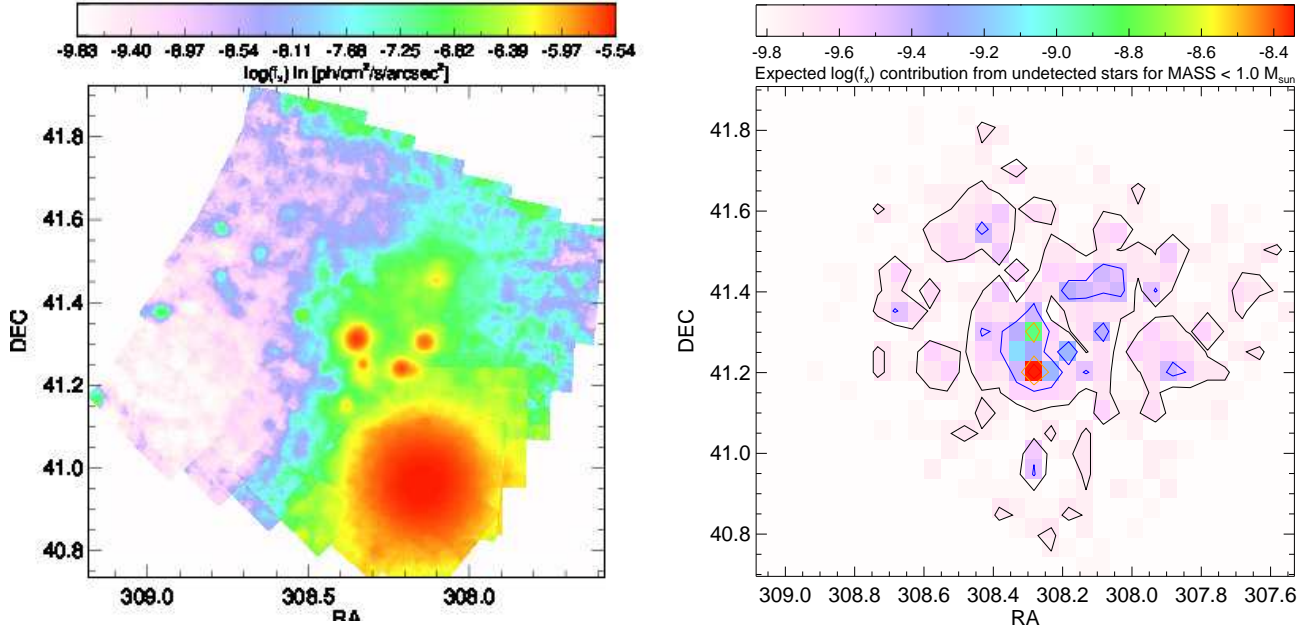
Figure 10. Left: The X-ray diffuse emission map for the full Cyg OB2 FOV in the [0.5-7.0] keV band. Right: Contours in log($f_{\text{unresolved}}$) indicating the intensity levels expected from the X-ray flux of unresolved stars.

$L_{uc}^{ONC} \sim 5.8 \times 10^{30}$ erg s^{-1}. At the distance of Orion (d $\sim$ 450 pc), and accounting for our CF [erg/ph], we obtained the expected flux per detected star, f_{uc}^{ONC}=4.5$\times 10^{-5}$ [ph/s/cm^2/star]. For COUP stars with a visual extinction $A_v \leq 5$ mag and masses below 1.0 M$_\odot$, we get a total population of 84 stars. Applying the same restriction for the Cygnus OB2 members, we find 786 stellar members with masses in the range [0.3 – 1.0] M$_\odot$. This implies that Cygnus OB2 is $\sim$9.2 times more massive than Orion for the same mass range. By adopting a distance of 1450 pc to Cygnus OB2, the total X-ray contribution for unresolved stars in the range [0.3–1.0] M$_\odot$ and over the entire observed area ($\sim$ 1deg^2) is f_{uc}^{CygOB2} $\sim$4.6$\times 10^{-6}$ [ph/s/cm^2/star]. In the left panel of Figure 10, we illustrate the Cygnus OB2 source density map binned at 0.05 deg^2, weighted by the expected X-ray flux contribution of undetected stars. Thus the expected flux, f_{uc}^{CygOB2}, should be divided by the unit of area adopted for binning, dens_area= $(0.05 \times 3600)^2$ [stars/arcsec^2]. Finally, for each detected low-mass star the expected X-ray flux emission from unresolved stars per arcsec^2 (f_x^{uc}) is f_{uc}^{CygOB2}/dens_area = 1.4$\times 10^{-10}$ [ph/s/cm^2/arcsec^2], i.e. (log(f_x^{UC}) = -9.84). Note the peak of the expected X-ray flux contribution is log(max(f_x^{UC}))= -8.34 [ph/s/cm^2/arcsec^2] and this occurs only in a single region of 0.05 deg^2 centered at RA=308.3 deg and DEC=41.2 deg (Figure 10-right). However, this value is overestimated because we made use of a completeness function computed from 120 ks simulations (Wright et al. 2015a), while at this central position our survey has a nominal summed exposure of $\sim$ 220 ksec, leading into a deeper source detection threshold.

With this estimation, and at the same time, by comparison with our X-ray diffuse emission map, computed using the same spatial binning of 0.05 deg^2 (see figure 10-right), the detected X-ray diffuse emission patterns in the survey are above log(f_x)$\approx$-8.2. Thus the contribution from the unre-

solved stellar population, in the worst case, remains a factor 2.5 fainter than the observed emission. For the vast majority of the survey area, it is at least an order of magnitude lower, confirming detected X-ray diffuse emission structures are real, and not affected by the contribution of X-ray emission from undetected low-mass stars of the region.

6. SPECTRAL ANALYSIS OF DIFFUSE X-RAY EMISSION

X-ray spectral fitting of diffuse emission is a difficult undertaking, and requires sufficient X-ray photons to provide meaningful constraints on the X-ray spectral model parameters. The most straightforward procedure is to increase the source extraction areas to gain larger signal-to-noise ratios. To this end, we tessellated the whole image mosaic in the [0.5-7.0] keV band to achieve surface brightness regions with S/N ratio greater than 60. Figure 11 shows the tessellate-generated image made using the Weighted Voronoi Tessellation (WVT) Binning code (Diehl & Statler 2006). These tessellated regions can be readily translated into region files and used to extract events within CIAO. In order to avoid the contamination produced by the bright background X-ray scattered halo of Cyg X-3, all tessellated regions within a 8 arcmin radius of its position (RA $\approx$ 20:32', DEC $\approx$ +40:57') were excluded from the spectral analysis. The choice of this distance was discussed earlier in Section 4.2. However, for some tessellated regions, even beyond 8 arcmin, the fractional X-ray contribution would produce marginal contamination in the diffuse X-ray spectra. We account for this issue in the spectral model fitting and subtract residual Cyg X-3 signal from the total [0.5-7.0] keV diffuse emission. The spatially resolved spectral fitting models and parameters are presented in Table 1.

The extraction of the X-ray spectrum for each tessellated region was achieved by using the specextract CIAO task from
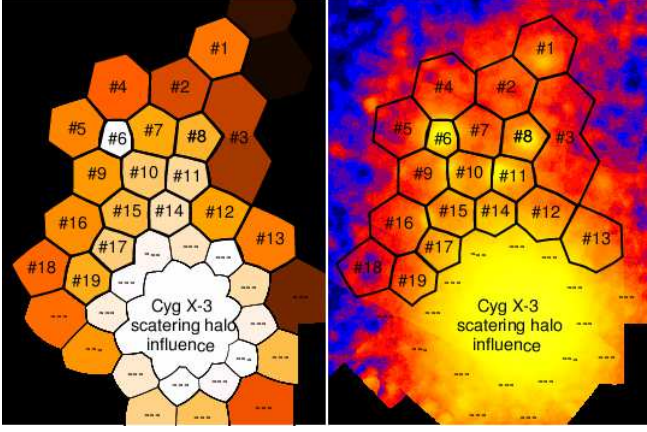
Figure 11. Left: Tessellated X-ray surface brightness of the Cygnus OB2 region. The achieved S/N is 60 and regions were computed to perform spatially-resolved X-ray spectral fitting. Regions labeled with dashed lines were not taken into account due to the influence of the background scattered X-ray radiation from Cyg X-3 (see discussion in section 4.2). Right: Diffuse X-ray mosaic events used for spectral extraction.

the respective diffuse event files. All spectra were properly weighted by the appropriate calibration files (the so-called ARFs and RMFs), that account for the many partially-overlapping ObsIDs. Background X-ray spectra were computed by using "stowed calibration events files". All X-ray spectra were grouped to reach a minimum Signal-to-Noise Ratio (SNR) per bin of 1, which produce unbiased best-fit values for the fitting procedure (Albacete Colombo et al. 2016).

For spectral fits, we used a suite of XSPEC spectral models (Arnaud 1996) to adequately account for possible combinations of emission components affected by equivalent hydrogen NH absorption column. The latter was included using the TBABS (Tuebingen-Boulder - TB) model (Wilms et al. 2000), that is composed by a combination of N(HI) (atomic hydrogen) and $2 N(H2)$ (molecular hydrogen). We tested the differences in the use of thermal emission models such as "PSHOCK" (PS), that is an averaged-abundance plane-parallel shock in non-collisional ionization equilibrium (NEI), and combination of "APEC" (AP) collisional ionization equilibrium (CIE) plasma models (Smith et al. 2001).

Unfortunately, the statistics of the spectra impose a limitation on the number of spectral models and free parameters that can be usefully constrained. We initially used the PS model to fit the softer ("Super-Soft" - SS) component (kT1), that gives short ionization timescales (from $\tau_u \sim 10^{-10}$ to 10^{-11} s cm^{-3}), implying a low-density highly non-equilibrum plasma (NEI). This interpretation supports intense and recent stellar winds and ISM shock interactions (Smith & Hughes 2010). Otherwise, "Soft" (S) and "Moderate" (M) energies were successfully described by two AP plasma models (kT2 and kT3) that adequately fit the observations for intermediate temperatures of each tessellated region. Finally, a fourth "Hard" (H) CIE plasma model (kT4) accounts for background non-resolved AGN—faint and hard—X-ray emission. Such a hard thermal component was able to match most of the hard diffuse emission, even though AGN are expected to be dominated by non-thermal emission and are usually well

modelled with power-law spectral shapes. However, the use of a thermal plasma spectral shape (kT4) may also be fitting more than just the unresolved AGN emission (Townsley et al. 2011a). Several attempts with simple (1T or 2T) models do not adequately fit the shape of the diffuse X-ray spectra, so we adopt a 4T combined model for spectral fitting, that is written with an XSPEC expression:

$$TB_1 \times PS_1 + TB_2 \times AP_2 + TB_3 \times AP_3 + TB_4 \times AP_4 \quad (1)$$

Models with variable abundance, e.g. "VPSHOCK" and "VAPEC", were not used as the number of free channels in the spectra is insufficient to discriminate adequately for differential abundance contributions from single elements. Otherwise, the fixed solar metal abundance pattern with scalable metallicity, Z, was not allowed to go below solar (Z= 1) as it is unlikely that massive star winds could produce sub-solar plasmas abundances (Strickland & Stevens 1998; Pittard & Parkin 2010). In fact, sometimes we slightly improved the goodness of the fit by allowing super-solar abundances, even if the actual abundance values were often not well-constrained, and/or eventually fixed. The spectral analysis was performed in an interactive way, with metallicity thawed, but carefully fitting in the restricted range of Z= 1.0–5.0.

For some tessellated regions (# 12, 13, 14, 17 and 19, see Table 1), the fourth hard (kT4) component helps us to disentangle the marginal contribution of the diffuse background ($\sim$ 9 kpc) scattering emission from Cyg X-3. In these cases, the absorption associated with the hard thermal component would be representative of a large total N_H absorption column, so it was initially set at 1.8×10^{22} cm^{-2}, but restricted in the fit to the range 0.8–10.0$\times10^{22}$ cm^{-2}.

The goodness-of-fit (χ^2/dof) obtained is generally acceptable (ranging from $\sim$1.0–1.1) for most of the tessellated regions. However, some cases of χ^2/dof $\sim$1.2–1.3 are probably associated with an ill-constrained emission model for scattered hard X-ray photons from the Cyg X-3 background radiation.

In Figure 12, we show of six example X-ray diffuse spectra that exhibit different spectral characteristics. In Table 1, we give the best-fit spectral parameters for the diffuse X-ray emission tessellated areas. Not surprisingly, three independent absorption models shape the apparent diffuse X-ray brightness of the region. For the stacked spectrum we get absorption values N_H^1, N_H^2, and N_H^3 of 0.43 (1σ=0.09), 0.80 (1σ=0.22), 1.39 (1σ=0.28) $\times10^{22}$ cm^{-2}, respectively, and temperatures of the components kT_1, kT_2 and kT_3 of 0.11(1σ=0.01), 0.42(1σ=0.08) and 1.21(1σ=0.18), respectively. This is direct evidence of the existence of a wide range of multi-temperature gas in the region. Otherwise, the hardest component is adequately described by a typical $N_H^4 \approx 2.7\times10^{22}$ cm^{-2} and a hard contribution from the unresolved AGN background population that can be represented by a $\sim$ 2.8 to 15 keV plasma.

Spectral analysis of the combined ("stacked") spectrum of the full region was performed using a four-temperature thermal input model. Results are consistent with those obtained from the averages computed for spatially-resolved spectra.
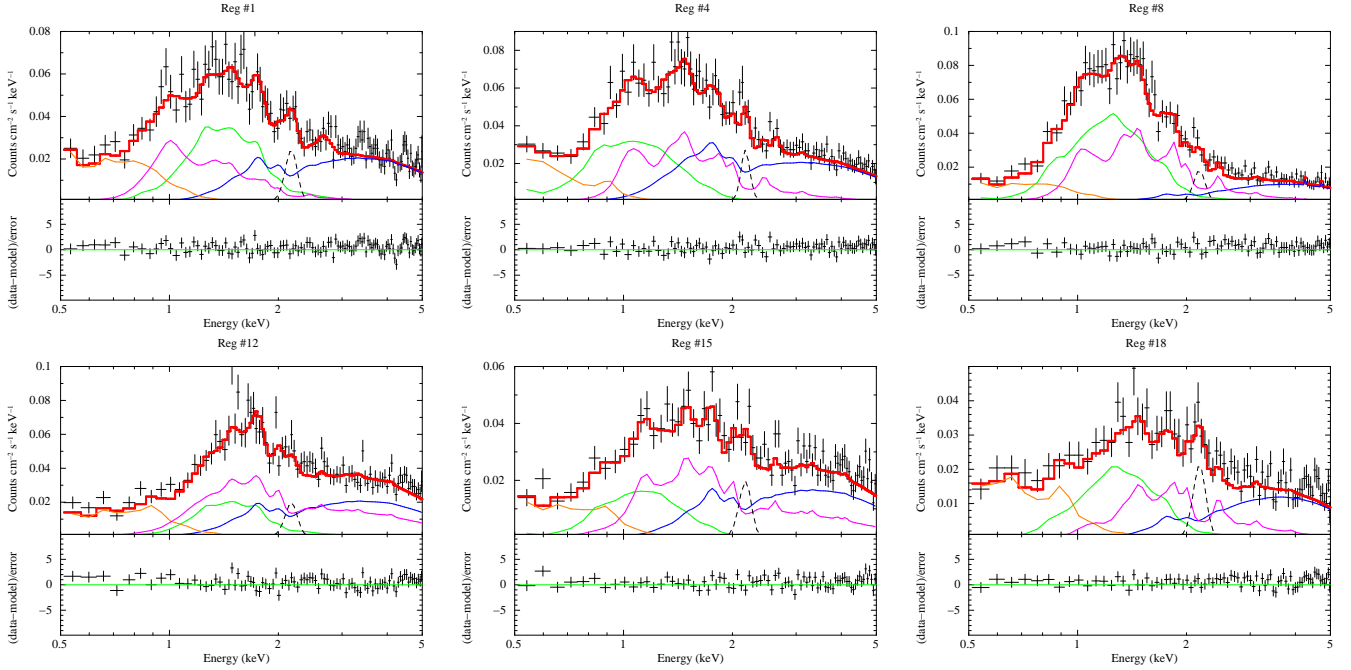
Figure 12. Sample of some tessellate spectra for regions- #1, 4, 8, 12, 15 and 18. Models that describe diffuse X-ray emission are indicated with red solid lines. The thinner colored lines represent the decomposition of the total emission into different models: Super-Soft (SS - orange), Soft (S - green), Moderate (M - Magenta) and Hard (H - blue). Note: Black dashed line correspond to the residual instrumental line at ~2.1 keV from background stowed spectra, which has not be taken into account for the event/stowed-bkg normalization (see 2.2 for discussion).
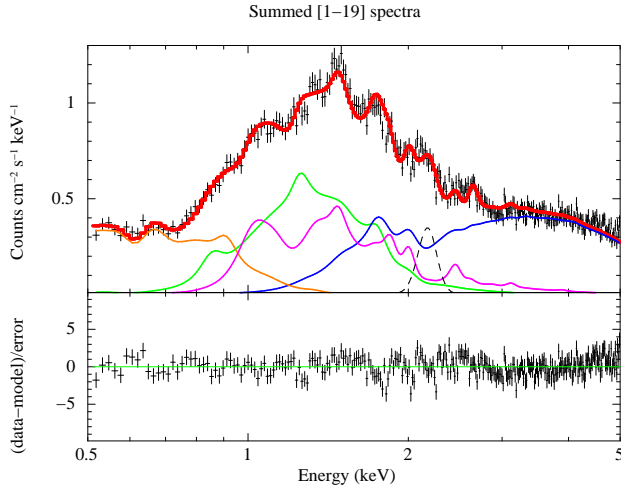

Figure 13. Stacked diffuse X-ray spectrum for the Cygnus OB2 region. The total ($0.5-7.0$ keV) diffuse X-ray fitted model (thick−red) has an intrinsic L_{tot} of 5.6×10^{34} erg s^{-1}. The total emission is decomposed into different models: Super-Soft (SS - in orange), Soft (S - green), Moderate (M - Magenta) and Hard (H - blue).

The total intrinsic diffuse X-ray luminosity is $L_x = 5.6 \times 10^{34}$ erg s^{-1} for the $0.5 - 7.0$ keV energy range. As shown in Figure 13, the total diffuse spectrum is successfully reproduced by a mix of the Super-Soft (SS)+ Soft (S) + Moderate (M) + Hard (H) plasma emission models. Unfortunately, there are also some regions of SS emission away from the centre of the Cygnus OB2 association that are too faint to construct tessellated regions for spectral extraction at S/N>1.

In contrast with the first three thermal components (SS, S and M), the H model appears highly absorbed ($\sim 2.6 \times 10^{22}$ cm^{-2}) and extremely hard (kT> 15 keV), as expected from the unresolved AGN background population and/or—for some cases—the scattered radiation from Cyg X-3. This hard component is then not part of the local diffuse X-ray emission of the region, so we have disentangled such component to estimate a background X-ray luminosity of L_x^H ($\sim 1.41 \times 10^{34}$ erg s^{-1}). Certainly, hard X-rays might originate in the Cyg OB2 association. In section 7.2 we discuss plausible non-thermal emission mechanisms present in the local diffuse X-ray emission of the region.

We consider the truly diffuse X-ray emission of the Cygnus OB2 region to be composed of the contribution from SS + S + M models, which have a total combined X-ray luminosity of $L_x^{diff} = 4.2 \times 10^{34}$ erg s^{-1} for the 0.5-7.0 keV energy range. The softer SS component is compatible with a temperature of 0.11 keV and an low absorption column of 0.42×10^{22} cm^{-2}, and which appears spatially related to the shock interaction between winds from massive stars and the local ISM (see section 7). Its relative contribution to the total X-ray diffuse emission of the region is ~37% ($L_x^{SS} \sim 1.52 \times 10^{34}$ erg s^{-1}), although owing to the scattered soft emission too faint for quantitative analysis mentioned above, the true SS flux could be larger. In fact, SS emission is just observed where absorption is low enough, being completely absorbed at other parts of the region. The S and M components, with respective temperatures of 0.40 and 1.18 keV, appear 2.8 to 3.2 times more absorbed (1.18 and 1.30 $\times 10^{22}$ cm^{-2}, respectively) than the SS emission. The S component contributes with the 46% ($L_x^S \sim 1.89 \times 10^{34}$ erg s^{-1}) and the M component 17% ($L_x^M \sim 0.69 \times 10^{34}$ erg s^{-1}) of the total diffuse X-ray luminosity of the region.

Table 1. Spectral model parameters of diffuse X-ray emission

Reg. #	Model	N_H [$\times10^{22}$ cm^{-2}] Diffuse / Bkg.	kT [keV] Diffuse / Bkg.	Norm. [cm^{-3}]	Z [$Z_\odot$]	Flux ($\times10^{-12}$ cgs) Diffuse / Bkg.	L_x ($\times10^{33}$ cgs) Diffuse / Bkg.
1	3T / bkg	$0.34-0.58-1.37/2.6$	$0.11-1.01-0.48/44.5$	0.26	1.3	6.07 / 3.13	1.52 / 0.78
2	3T / bkg	$0.50-0.59-1.53/2.6$	$0.10-0.76-0.42/34.4$	0.40	1.7	10.9 / 2.99	2.74 / 0.75
3	3T / bkg	$0.46-1.05-1.67/5.8$	$0.11-1.24-0.50/[64.0]$	0.56	3.4	29.2 / 9.12	7.34 / 2.29
4	3T / bkg	$0.33-0.50-1.35/1.6$	$0.09-0.31-1.23/[64.0]$	0.11	1.7	5.80 / 2.75	1.46 / 0.69
5	3T / bkg	$0.44-1.04-1.48/5.6$	$0.12-1.22-0.47/56.1$	0.23	3.7	11.79 / 3.01	2.96 / 0.75
6	3T / bkg	$0.57-1.00-1.05/[10]$	$0.13-0.56-1.21/13.7$	0.13	2.1	6.77 / 1.76	1.71 / 0.44
7	3T / bkg	$0.18-0.66-0.98/2.7$	$0.08-0.91-0.42/[64.0]$	0.23	1.4	3.34 / 2.13	0.85 / 0.53
8	3T / bkg	$0.33-0.80-1.39/4.6$	$0.11-0.38-1.02/57.3$	0.12	2.1	7.25 / 1.86	1.82 / 0.46
9	3T / bkg	$0.29-0.76-1.44/2.8$	$0.11-0.39-1.08/[60]$	0.11	2.1	4.26 / 2.32	1.07 / 0.58
10	3T / bkg	$0.45-1.23-1.38/4.5$	$0.13-1.21-0.46/43.3$	0.14	1.6	7.44 / 2.74	1.87 / 0.68
11	3T / bkg	$0.44-1.00-1.36/4.2$	$0.10-1.11-0.51/42.7$	0.44	1.9	6.69 / 2.37	1.68 / 0.59
12†	2T / Cyg X-3+bkg	$0.49-0.97/1.7-2.7$	$0.12-0.45 /11.4-[64]$	0.25	3.8	9.31 / 3.15	2.34 / 0.79
13†	2T / Cyg X-3+bkg	$0.40-0.71/2.9-2.6$	$0.11-0.53/10.8-[64]$	0.26	1.8	9.30 / 2.87	2.33 / 0.72
14†	2T / Cyg X-3+bkg	$0.52-1.60/2.9$	$0.10-0.41/61.8$	0.27	1.1	9.96 / 3.16	2.50 / 0.79
15	3T / bkg	$0.43-0.74-0.83/2.6$	$0.10-0.27-5.7/39.8$	0.26	3.8	5.25 / 2.56	1.32 / 0.64
16	3T / bkg	$0.38-0.80-1.81/3.4$	$0.11-0.38-0.68/7.8$	0.16	1.8	5.97 / 5.02	1.51 / 1.26
17†	2T / Cyg X-3+bkg	$0.50-1.86/2.6$	$0.11-0.51/10.8$	0.50	1.7	5.26 / 2.90	1.33 / 0.72
18	3T / bkg	$0.34-0.98-2.38/4.1$	$0.13-0.44-1.21/27.4$	0.04	1.7	5.46 / 2.38	1.37 / 0.59
19†	3T / Cyg X-3+bkg	$0.38-1.26-1.61/2.6$	$0.11-0.32-1.26/[64]$	0.29	3.9	14.6 / 2.66	3.67 / 0.66

Stacked	Model	N_H-components	kT-components	Norm.	Z	Flux	L_x	% Diff.
SS	Super-Soft	0.43 ± 0.09	0.11 ± 0.01	2.53	1.3	60.4 ± 7.5	15.2 ± 1.9	37 ± 3
S	Soft	0.80 ± 0.22	0.40 ± 0.08	1.79	1.8	75.1 ± 10.1	18.9 ± 2.7	46 ± 5
M	Moderate	1.39 ± 0.28	1.18 ± 0.18	0.43	3.1	31.0 ± 5.1	7.8 ± 1.3	17 ± 2
H	Hard	2.70 ± 0.42	45 ± 19	0.09	1.0	56.0 ± 16.7	14.1 ± 4.2	$--$
Diffuse	SS+S+M			4.76	[1.2]	166.7 ± 26.1	41.95 ± 6.6	100

The "bkg"—the hardest component of the diffuse emission spectra—refers to the contribution from unresolved AGN background emission. A thermal model approximation is sufficient to describe the hard emission (see text for discussion). The column 5 (Norm.) and 6 (Z) refers to the normalization parameter and the abundance of the model, respectively. The presence of diffuse non-thermal emission is addressed in Section 7. Both flux and luminosity were computed for the 0.5 - 7.0 keV energy range. † refers to spectra affected by Cyg X-3 scattered photons, which were also modelled by a thermal component. Last column of the bottom table indicates the percentage of SS, S and M contribution to the total diffuse X-ray emission.

7. DISCUSSION

This work has demonstrated, for the first time, the existence of true diffuse X-ray emission in the Cygnus OB2 stellar association. It is of interest to examine possible mechanisms responsible for the observed diffuse emission and its spatial morphology, which is probably related to a mix of different, thermal and/or non-thermal, physical mechanisms acting separately, but sharing a single spatial region. In Figure 14 we show a global view of the diffuse X-ray emission that is dominated by a mix of soft [0.5 – 1.2] keV and intermediate hardness [1.2 – 2.5] keV X-rays, in agreement with three thermal contributions that we obtained from spectral analysis. The 2.5 – 7.0 (hard) keV energy band is instead largely dominated by the background contamination (see section 4.1) and/or, in some regions, scattered radiation from Cygnus X-3 (see section 4.2).

7.1. *Thermal contribution to diffuse X-ray emission*

The diffuse emission closely follows the spatial distribution of massive stars (Wright et al. 2015b). The most widely accepted physical mechanism for production of diffuse hot gas is by multiple interactions of the winds from massive stars with the ambient ISM (e.g., Cantó et al. 2000). This kind of ISM–wind interaction occurs under the action of stellar wind momentum so as to produce low ISM densities, such that the X-ray diffuse gas would be characterized by high-pressure (low ISM density) and high temperature. However, it is remarkable that the Soft [0.5–1.2] keV contribution, which is somewhat fainter than intermediate energy band emission, appears much more dispersed and also less confined at the locations of evolved massive stars. This result suggests that the cumulative influence of intense massive stellar winds act to fill and heat the surrounding ISM, injecting enough thermal energy to drive outward via expanding turbulent diffusive motions of hot gas on scales of several parsecs, even in places absent of massive stars (Dwarkadas & Rosenberg 2013).

According to simple theoretical scaling approximations (Stevens & Hartwell 2003), part of the stellar wind kinetic energy is thermalized, so we can derive a simple estimate for the expected temperature of the shocked gas (T_{shock}) $\approx 1.3\times10^7 (v_w/1000)^2$ in K, where v_w is the typical stellar wind velocity of massive stars in units of km s^{-1}. For massive stars the stellar wind expansion obeys a β-law velocity, $v(r) = v_\infty(1 - R_\star/r)^\beta$, with β=0.8 for super-sonic winds
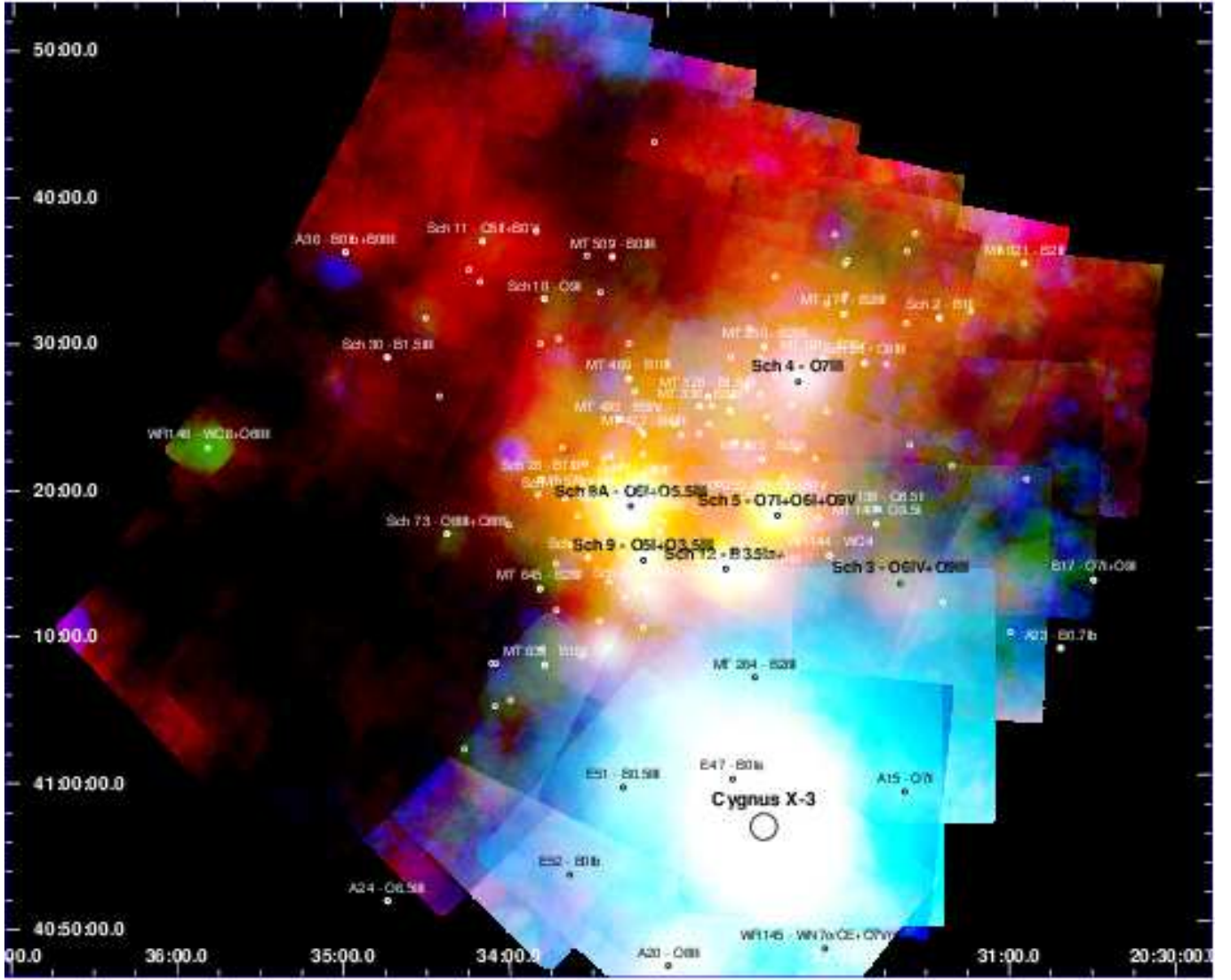
Figure 14. The Cygnus OB2 diffuse emission map in the $0.5 - 7.0$ keV band. The full band is coded in color so that soft $[0.5 - 1.2]$ keV emission appears in red, and medium $[1.2 - 2.5]$ keV in green, while hard $[2.5 - 7.0]$ keV emission appears in blue. Small white circles indicate the massive stellar content of the region. Names and labels indicate the evolved stars with more intense stellar winds. Names are omitted for main sequence O- and B-type stars that have less massive winds. The X-ray mosaic intensity is logarithmically scaled, and the region shown is approximately 1.3×1.3 degrees, with North up and East to the left.

(Pauldrach et al. 1986), thus for distances greater than 10 times the stellar radius ($10 R_\star \leq 0.01$ pc) the ratio $v_w/v_\infty \geq 0.95$, so v_w is well approximated with typical v_∞ values. The stellar terminal wind velocity of early O-type stars ranges from 900 to 2800 km s^{-1} so gas temperatures would range between 1.0 and 10.1×10^7 K, which is equivalent to energies of ~ 0.9 to 8.7 keV. While these energies are roughly consistent with what we observe, they should be considered as upper-limits because T_{shock} here is computed as a purely radiative limit. In a more realistic description, it is expected that a fraction of energy released from the winds of massive stars deposits mechanical energy into the ISM.

The entire massive stellar content of the Cygnus OB2 region comprises: *i*) 25 evolved (of Classes I, Ie, II((f)), III) massive stars of O-type, plus 4 Wolf-Rayet stars; *ii*) 28 evolved B-type stars of classes I, Ia, Ib, II, III, most of them characterized by slow winds and faint, or absent, intrinsic

X-ray emission; *iii*) 113 O-type and early B-type stars on the main sequence (Wright et al. 2015c). The contribution to the total stellar wind energy L_w released by each star can be obtained according to the expression $3 \times 10^{35} \dot{M}_{-6} (v_w/1000)^2$ in erg s^{-1}, where $\dot{M}_{-6}$ is the mass loss rate in units of $10^{-6} M_\odot$ yr^{-1}, (Cantó et al. 2000). We adopted individual mass loss rates according to the Vink et al. (2001) formalism and terminal wind velocities assumption of $v_\infty = 2.6\, v_{\mathrm{esc}}$ (Lamers et al. 1995), which were computed by Rauw et al. (2015) for the entire massive star population of the region. The total L_w released by each one of these three groups separately is $\approx 1.3 \times 10^{38}$, 6.6×10^{36}, and 1.3×10^{37} erg s^{-1}, respectively. The total stellar wind energy injected into the ISM of the region, from the entire population of massive stars, is then $\approx 1.5 \times 10^{38}$ erg s^{-1}, with the evolved O stars dominating.

At this point, it is interesting to estimate the kinetic to diffuse X-ray emission efficiency by computing the diffuse
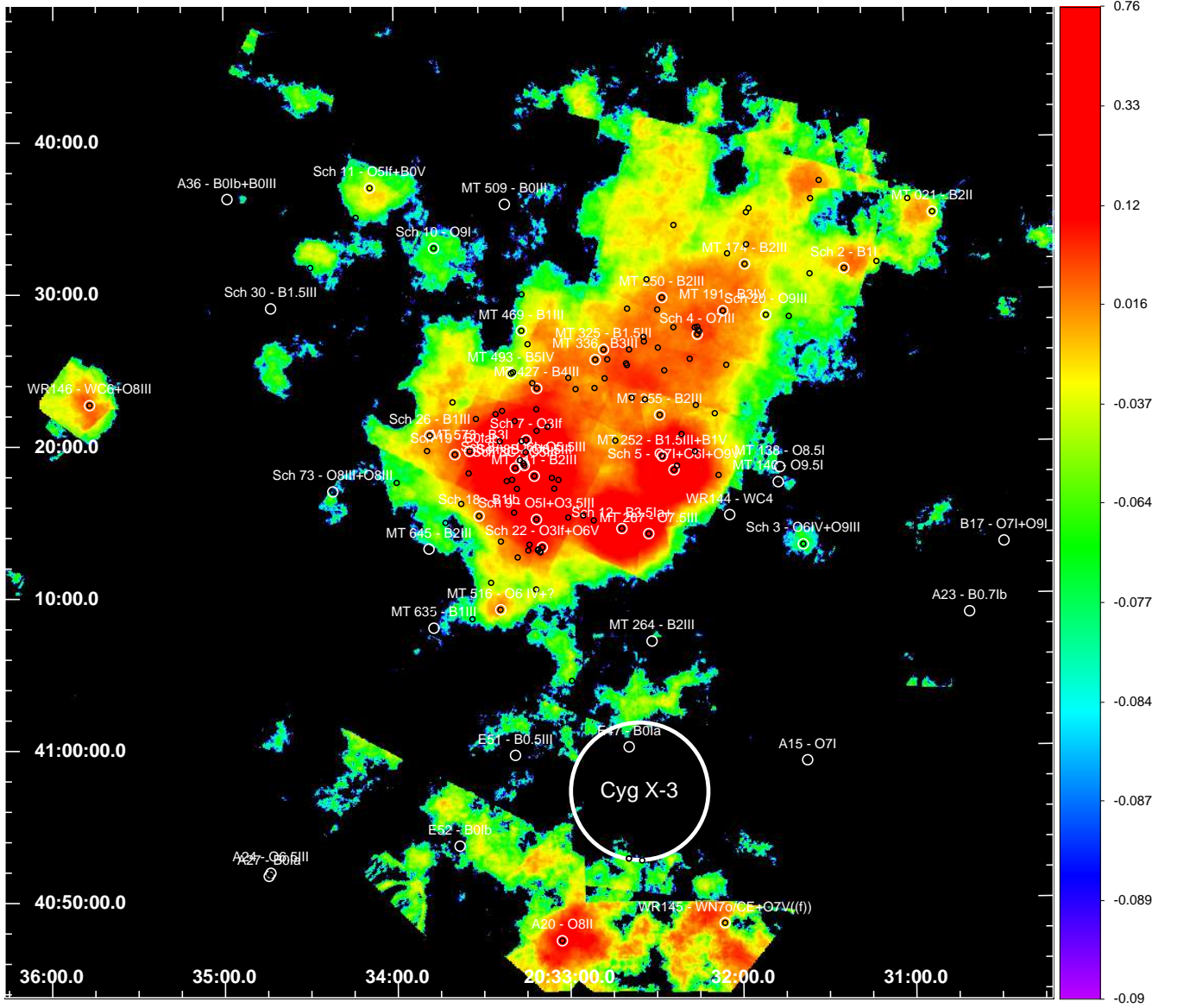
Figure 15. The Cygnus OB2 hardness ratio (HR) diffuse map in the soft [0.5 – 2.5] keV and hard [2.5 – 7.0] keV bands. Spatial regions of diffuse gas that correspond to HR values lower than −0.1 were discarded (see section 4). Small black circles indicate the MS massive stars of the region. Names and labels in white indicate the evolved stars with more intense stellar winds (Wright et al. 2015b). Names are omitted for main sequence O- and B-type stars that have less massive winds. The X-ray mosaic intensity is logarithmically scaled.

X-ray luminosity of the region. Early works based on the CWM have provided some reliable estimates for the X-ray diffuse emission in massive SFRs, e.g. R136 and NGC 3603 (Moffat et al. 2002), NGC 346 (Nazé et al. 2002), Rosette (Townsley et al. 2003), and Westerlund I (Muno et al. 2006). They have found that the diffuse X-ray luminosity in the broad band of 0.5–8.0 keV usually lies in the range (1-6) $\times 10^{34}$ erg s^{-1}. Such estimates indeed confirm the efficiency $L_x^{diff}/L_w \sim 2\times10^{-4}$, as predicted by Dorland & Montmerle (1987) through the investigation of dissipative mechanisms. Now, if we assume that the diffuse X-ray emission luminosity is entirely produced through wind shock–ISM dynamical interaction, the efficiency in Cygnus OB2 is $\eta \sim L_x^{diffuse}/L_w = 4.2\times10^{34}/1.5\times10^{38} = 2.8\times10^{-4}$, or about a factor ~ 2 more

efficient than in Westerlund 1 (Wd 1).

Next, we are able to estimate the diffuse X-ray luminosity via the CWM model. Such a model assumes that the bulk of the diffuse emission in the region is due to a hot plasma that exhibits relaxed, center-filled morphology with a lack of any obvious, measurable temperature gradients. We therefore considered the simple hypothesis of uniform, optically thin thermal plasma with a simple geometry, although the emission doubtless has a more complex structure in reality. As discussed in section 4, thermal diffuse emission is an adequate description if we adopt diffuse emission regions with HR below - 0.1. Figure 15 shows this diffuse emission with regions of harder emission removed.

The total mass of hot gas (HR≥-0.1) in the region that emits

in X-rays covers overly precise $\sim$35 % of the total survey area of ≈ 0.97 sq-deg, which at the distance of 1450 pc to Cygnus OB2, corresponds to an area of 209.5 pc^2. This area is equal to a 14.5$\times$14.5 parsec side (s_x) square. Because stellar wind–ISM interaction occurs in a three-dimensional (3D) space, the observed bi-dimensional (2D) diffuse gas density in (cm^{-2}) cannot directly be compared with gas density in cm^{-3} units. We therefore converted the observed 2D to 3D geometry, by conservation of the total mass−−square area equal to sphere surface−−of a 2D circle to a 3D sphere of the diffuse gas that radiates in X-rays. Thus the area $s_x^2=4.\pi R_c^2$, where R_c is the cluster effective radii. This equation gives a R_c of ~ 4.1 pc ($\sim$ 0.16 deg), so the characteristic plasma volume of the region is $V_x=4/3\pi R_c^3 = 8.48\times10^{57}$ cm^{-3}. Using the CWM and the analytic solutions to the density (n_0) in cm^{-3} (see equation 4 of Cantó et al. (2000)), we find n_0=0.06 cm^{-3} that is the typical mass density contribution from massive stellar winds in the region.

The emission measure of the diffuse X-ray emission is obtained by integration of electron density squared over the emitting volume (EM = $3/4\pi R_c^3 n_0^2$), thus EM $\sim 1.71\times10^{55}$ cm^{-3}, and XSPEC normalization (Norm = 10^{-14} EM/$(4\pi D)^2$) of 3.9. With all these parameters, and assuming that the emission is well described by a combination of three thermal plasmas (see section 6), we simulated a fake X-ray spectrum by assuming APEC models at temperatures kT$\approx$ 0.1, 0.4 and 1.2 keV (see table 6). In order to compute theoretical absorption-corrected X-ray luminosity, we applied individual multiplicative neutral Hydrogen absorption column (using TBabs) to the emission models, Values of N_H=0.42, 1.1, and 1.3×10^{22} cm^{-2} were obtained from our X-ray spectral fitting results (see sub-section 6). It should be mentioned that if we adopt the dust column density relationship N_H/A_v=1.6$\times10^{21}$ cm^{-2}, which represents the better proxy for the soft X-ray absorption column density from HI maps (Flaccomio et al., this issue), the A_v in the region ranges between 2.6 and 6.8 mag, values which are consistent with the median of value 4.5 mag (Guarcello et al. this issue). Using these approaches, we predict a theoretical soft X-ray luminosity L_x^{Soft}=2.1$\times10^{34}$ erg s^{-1}, and hard L_x^{Hard}=0.2$\times10^{34}$ erg s^{-1}, leading to a total diffuse X-ray luminosity L_x^{diff} of 2.3$\times10^{34}$ erg s^{-1}, for the 0.5-7.0 keV energy band, a factor $\sim$2 lower than spectral fit results. In any case, and for different reasons, diffuse X-ray luminosity computed from spectral fitting or from CWM, should be more rigorously considered a lower limit.

Comparing our X-ray flux estimate to that of other SFRs, we find the diffuse X-ray luminosity in Cygnus OB2 is a factor $\sim$3 larger than that estimated for the Arches cluster (1.6$\times10^{34}$ erg s^{-1}, Yusef-Zadeh et al. (2002)); $\sim$2 times larger than for the massive NGC 3603 cluster (2.0$\times10^{34}$ erg s^{-1}, Moffat et al. (2002)); but $\sim$7 times fainter than computed for the Carina Nebula (3.2$\times10^{35}$ erg s^{-1}, Townsley et al. (2011a)) for the same energy band. These agreements support the idea that the massive stellar content plays a major, but proportional, role in the efficiency of conversion from injected kinetic wind energy through ISM interaction to the diffuse X-ray luminosity, that for Cygnus OB2 is $\sim 3\times10^{-4}$.

However, it is plausible that non-thermal processes may be acting efficiently near the massive stars, altering, and perhaps increasing, the diffuse X-ray luminosity of the region. Thus, it is of interest to examine potential non-thermal emission contributions and their implications in a multi-wavelength context.

7.2. *Non-thermal contribution to diffuse X-ray emission*

Diffuse X-ray emission may also be produced through non-thermal mechanisms. Evidence for non-thermal processes has been uncovered in the Westerlund 1 star cluster by Muno et al. (2006). However, those authors suggested that about 30% of the diffuse X-ray emission continuum would be produced by the unresolved Pre Main Sequence star (PMSs) population in the region, probably through magnetic reconnection flares and/or micro-flares. The relevant non-thermal emission processes are Synchrotron Losses (SL) and Inverse Compton (IC) scattering, which naturally produce more hard ($\geq$ 2 keV) X-rays, and are consequently not trivially distinguishable from the AGN background diffuse contribution. A third process, leading to softer X-rays, is Charge Exchange (CXE) line emission. The relative importance of these mechanisms depends on how, and where, the required population of non-thermal particles are created in the region, the neutral Hydrogen density of the local ISM, and also the local magnetic field in the region.

In order to compare relative SL and IC loses, we compute the ratio between the radiation field density (U_{ph}) of massive stars of the region and the expected ISM magnetic density ($U_B=B^2/8\pi$) of the region. We adopted a typical ISM magnetic field of B$\sim$4 μG (Beck 2001) to calculate U_B and used the individual bolometric luminosity (L_7) to compute U_{ph} (= 5.5$\times10^{-9}L_7 d_{pc}^{-2}$) in erg cm^{-3} around each massive star (Muno et al. 2006). The individual U_B/U_{ph} ratio as a function of distance (d_{pc}) for each massive star was calculated, but for simplicity Figure 16 only shows the median and integrated U_{ph} as a function of distance from the stars. The averaged $U_{B=4\mu G} \geq U_{ph}$ condition is supplied for distances above 0.5 pc and 1 pc for single main sequence (MS) and evolved massive stars, respectively. We considered the projected density of massive stars in the region, which has a typical value of 0.8 star/pc^2, so the respective contributions to U_{ph} from individual massive stars should be added to get a more realistic estimation of the U_{ph}. The radiation field hypothetically has a maximum at the centre of the diffuse X-ray emission –in agreement with the spatial density of massive stars– (centred at RA= 20:33:00 , DEC=41:20:00), see Figure 15. Figure 16 shows that SL becomes important only for distances larger than $\sim$ 5 pc ($\sim$ 12.4 arcmin) from the centre of the region. However, at such a distance, the observed diffuse X-ray emission is absent, or just marginally detected in soft X-rays, so that synchrotron losses would not be contributing significantly to the observed X-ray diffuse emission.

Otherwise, Inverse Compton (IC) scattering is a potential loss term for diffuse X-ray emission, feeding off copious UV photons from massive stars. However, the dilution of the UV field (U_{phot}) increases with the distance to the stellar source, and thus rapidly decreases the energy of the electrons after they leave the vicinity of the shock, imposing a natural "short"
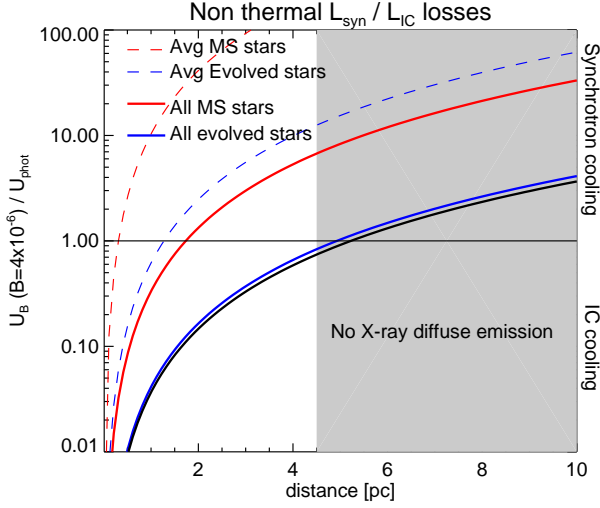
Figure 16. Curves representing the expected relative contribution of synchrotron to inverse Compton loses to the diffuse X-ray emission. The black continuous line corresponds to the ratio $U_{B=4\mu G} / U_{ph}$ accounting for the total contribution from all massive stars of the region with respect to the centre of the diffuse emission. The coloured grey region represents distances from the adopted centre (RA= 20:33:00, DEC=41:20:00) in which diffuse X-ray emission is not observed.

distance restriction for the action of this mechanism. So, considering that the luminous (evolved) stars shock occurs in the radiative cooling limit, we compared synchrotron to IC loses through the expression $L_{syn}/L_{IC} = U_B/U_{phot} \approx 7.1 \times 10^{-4} B^2/L_6$, where $B=B_{star}(v_{rot}.R/v_\infty)d^{-1}$ and L_6 in $10^6 L_\odot$ (White & Chen 1995). As U_{syn} and U_{phot} go as the inverse square of the distance, and adopting typical values for the magnetic fields of the massive stars ($B_{star} \sim 200$ G), $L_{syn}/L_{IC} \approx 10^{-7}$, so the IC process is dominant over SL near the massive stars. However, the energy requirement to raise the input energy of UV photons ($E_{input} \sim 10$ to 20 eV) into the observed X-ray regime of the diffuse emission (E_{out} in 0.5 - 7.0 keV) requires a population of accelerated electrons of moderate energy ($\sim$ 5-35 MeV) generated in the inner wind of massive stars, or even from colliding wind regions (Muno et al. 2006). So IC cooling may act in the inner stellar winds and cannot travel far from the acceleration site (Chen 1992; Eichler & Usov 1993); thus, large-scale (few parsecs) IC cooling is not expected to contribute to the observed diffuse X-ray emission.

These theoretical predictions for insignificant contributions from synchrotron losses and inverse Compton scattering therefore agree with the observed absence of hard [2.5 - 7.0] keV diffuse X-ray emission (Figure 14).

Alternatively, there is one further mechanism that could produce non-thermal diffuse X-ray emission. Theoretical (Wise & Sarazin 1989), and more recently observational (Townsley et al. 2011a), considerations suggest highly charged ions associated with hot plasma (from massive stellar winds) could interact with neutral atoms of ambient cool or warm ISM gas via the Charge X-ray Exchange (CXE) mechanism. CXE is a non-thermal line emission mechanism that could produce conspicuous diffuse X-ray emission at soft (line-emission) energies, even when such interactions occur on spatial scales of several tenths of

parsecs (Montmerle & Townsley 2012). Calculations from Wise & Sarazin (1989) have shown that CXE emission is negligible in the case of Supernova Remnants with fast shocks, but becomes important for less energetic cases, such as hot gas interacting with cold, dense ISM structures. The process is more efficient for lighter elements (Lallement 2004) and a wide variety of emission lines below 2 keV are expected from elements in various ionization states, with no continuum contribution. In Carina, for example, lines and possible elements responsible for them are 0.64 keV (O), 0.77 keV (O or Fe), 1.07 keV (Ne), 1.34 + 1.54 keV (Mg), 1.80 keV (Si), and some faint lines at harder X-ray energies such as 2.61 keV (S), and 6.50 keV (Fe) (Townsley et al. 2011a). Such emission has been also suggested in other massive star-forming regions for which the data were of sufficient quality (Townsley et al. 2011b). In Figure 17 we inspected the neighbourhood of Cygnus OB2 in a multi-wavelength approach, by searching for plausible regions for CXE emission, where soft X-ray diffuse emission co-exists with "warm" ($\approx$ 100-150 K) and cold ($\approx$ 10-50 K) gas structures observed in the infrared (*Spitzer* and Herschel data, respectively). Just four zones satisfy this condition, one to the north and the other toward the center of the region. However, soft diffuse emission luminosity in these three regions is low enough to search for narrow band images at excesses produced by CXE emission line energies, e.g. ~[0.6-0.8] keV for O and/or Fe lines; ~[1.0-1.6] keV for Ne and/or Mg. Although the poor photon statistics in the X-ray spectra of these regions do not allow us confirm the presence of line emission from He-like and H-like states of the elements C, N, and O, the mere existence of soft diffuse X-ray emission, even far from the massive stars, would be considered a favorable place for the CXE mechanism occurring in Cygnus OB2.

The multi-wavelength image of the region (see Figure 17) also shows that most X-ray diffuse emission is spatially coincident with regions of low infrared surface brightness, which is in coincidence with regions of low ISM extinction. This suggests the X-ray plasma is volume-filling, rather than edge-brightened, just as was found for the Carina Nebula (Townsley et al. 2011a) and other giant H II regions (Townsley et al. 2011b). This is an indirect observational probe that in the case of Cygnus OB2, powerful stellar winds from massive stars primarily collide between the OB winds rather than independently with the exterior cold cloud, which is in concordance with Cantó et al. (2000) 3D modelling of SFRs with high density population of massive stars.

Finally, and for the first time, we have resolved X-ray diffuse emission haloes at sub-parsec scales around some evolved massive stars of the region (see figures and respective comments in the Appendix). We defer a more detailed study of this phenomenon to future work.

8. SUMMARY

A thorough and detailed analysis of 40 *Chandra* ACIS-I observations of the Cygnus OB2 Association, including the removal of the 7924 X-ray point-like sources detected, has re-
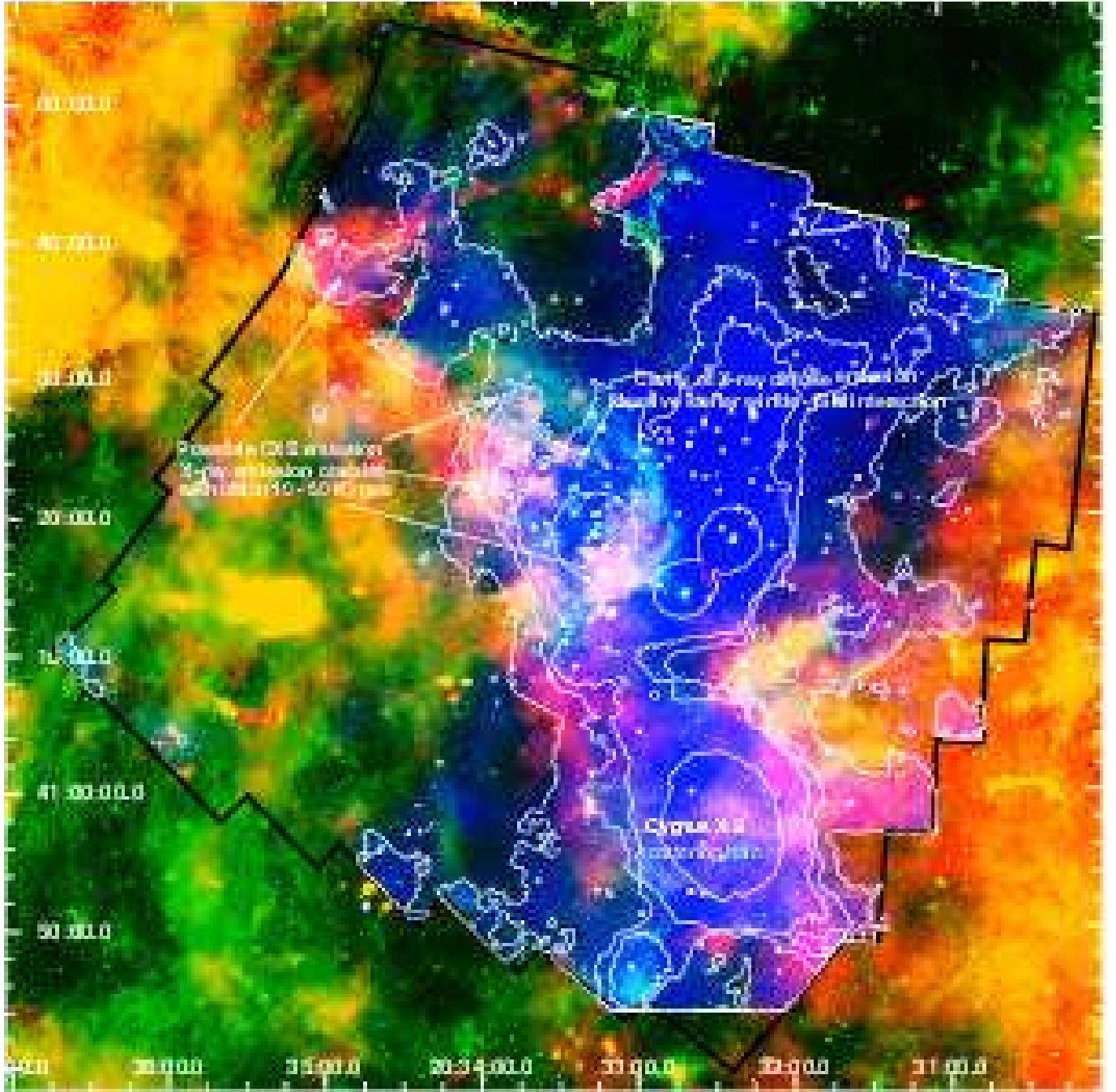
Figure 17. The neighbourhood of Cygnus OB2. The ACIS-I mosaic of the Cygnus OB2 survey is outlined in black. Small circles indicate the massive OB star content of the region, regardless of spectral type and evolutionary class (Wright et al. 2015b). Diffuse X-ray contours corresponding to flux levels of 3.0, 3.7, 4.1, 4.7 and 8.3 $\times10^{-10}$ ph/cm^2/s/arcsec^2, are shown in white. The false RGB color image was composed as follows: The Herschel 500 μm (T $\approx$ 10 K) cold gas emission in red (Schneider et al. 2016), the 8 μm Spitzer IRAC image for the warm gas (T $\approx$150 K) in green, and the diffuse X-ray emission in the 0.5 – 2.5 keV energy range in blue. There are also four arrows that indicate the regions which show signs of the coexistence of 10 K cold ISM gas and hot diffuse X-rays, which are likely scenarios for CXE emission.

vealed the diffuse X-ray emission that permeates the region. We have mapped a region $\sim$ 30 pc^2 across at a spatial resolution reaching down to a few thousand of AU. The main findings of the study of this diffuse emission are as follows.

1. Large-scale X-ray diffuse emission was seen in the broad 0.5 – 7.0 keV energy band, and was also detected in the Soft [0.5 : 1.2] and Medium [1.2 : 2.5] keV bands.

A marginal detection of diffuse emission was made in the Hard [2.5 : 7.0] keV band.

2. The total diffuse X-ray emission luminosity was found to be L$_x^{\text{diff}}$ $\approx$4.2$\times10^{34}$ erg s^{-1} (0.5-7.0 keV), and was well-represented by a three-component thermal plasma model with typical temperatures of kT$\approx$ 0.11, 0.40 and 1.18 keV (1.2, 4.9 and 14 MK, respectively).

3. The extended moderate energy emission likely arises from O-type star winds thermalized by wind-wind collisions in the most populated regions of the association, while the Super-Soft (SS) emission probably arises from less energetic termination shocks against the surrounding interstellar medium (ISM). The SS diffuse emission appears more dispersed than that at soft and medium energies, indicating diffusive motions of hot gas on 2 to 3 parsec scales.

4. The HI absorption column density was constrained with three individual N_H models, that on stacked spectra are N_H = 0.42, 1.12 and 1.30 $\times 10^{22}$ cm^{-2}. At the center of the region, where most of the massive stars are located, N_H seems to be slightly lower than found for outer regions. The diffuse X-ray emission is then spatially coincident with low extinction regions (and low ISM densities), that we attribute to powerful stellar winds from massive stars and their interaction with the local ISM. It is volume-filling, rather than edge-brightened, as has been found for other star forming regions.

5. An assessment of potential non-thermal diffuse emission sources finds that both synchrotron and inverse Compton scattering are not likely to contribute significantly to the observed large scale diffuse emission. A full assessment of a possible charge-exchange emission signal is challenging due to the large extinction that renders soft X-ray emission difficult to observe. By the way, this would require a more detailed spectral analysis.

6. Examination of the diffuse emission maps on smaller scales reveals X-ray halos around evolved massive stars. This is the first time such emission structures have been detected.

The results presented here highlight the value of large-scale X-ray surveys for understanding the energetics and feedback in massive star-forming regions, in addition to assessing their otherwise hidden or inconspicuous stellar content.

REFERENCES

Albacete Colombo, J. F., Flaccomio, E., Drake, J. J., et al. 2016, ArXiv e-prints

Albacete Colombo, J. F., Flaccomio, E., Micela, G., Sciortino, S., & Damiani, F. 2007, A&A, 464, 211

Arnaud, K. A. 1996, in Astronomical Society of the Pacific Conference Series, Vol. 101, Astronomical Data Analysis Software and Systems V, ed. G. H. Jacoby & J. Barnes, 17

Beck, R. 2001, Space Sci. Rev., 99, 243

Broos, P., Townsley, L., Getman, K., & Bauer, F. 2012, AE: ACIS Extract, Astrophysics Source Code Library

Bruhweiler, F. C., Freire Ferrero, R., Bourdin, M. O., & Gull, T. R. 2010, ApJ, 719, 1872

Butt, Y. M., Drake, J., Benaglia, P., et al. 2006, ApJ, 643, 238

Cantó, J., Raga, A. C., & Rodríguez, L. F. 2000, ApJ, 536, 896

Cash, W., Charles, P., Bowyer, S., et al. 1980, ApJL, 238, L71

Chen, W. 1992, PhD thesis, Johns Hopkins Univ., Baltimore, MD.

Comerón, F., Pasquali, A., Rodighiero, G., et al. 2002, A&A, 389, 874

Corral, A., Della Ceca, R., Caccianiga, A., et al. 2011, A&A, 530, A42

Diehl, S. & Statler, T. S. 2006, MNRAS, 368, 497

Dorland, H. & Montmerle, T. 1987, A&A, 177, 243

Drew, J. E., Greimel, R., Irwin, M. J., & Sale, S. E. 2008, MNRAS, 386, 1761

Dwarkadas, V. V. & Rosenberg, D. L. 2013, High Energy Density Physics, 9, 226

Eichler, D. & Usov, V. 1993, ApJ, 402, 271

Feigelson, E. D., Getman, K., Townsley, L., et al. 2005, ApJS, 160, 379

Fruscione, A. 2014, Chandra News, 21, 24

Getman, K. V., Broos, P. S., Feigelson, E. D., et al. 2011, ApJS, 194, 3

Getman, K. V., Feigelson, E. D., Grosso, N., et al. 2005, VizieR Online Data Catalog, 216, 353

Guarcello, M. G., Drake, J. J., Wright, N. J., et al. 2016, ArXiv e-prints

Güdel, M., Briggs, K. R., Montmerle, T., et al. 2008, Science, 319, 309

Hanson, M. M. 2003, ApJ, 597, 957

Hickox, R. C. & Markevitch, M. 2006, ApJ, 645, 95

Koljonen, K. I. I., Hannikainen, D. C., McCollough, M. L., Pooley, G. G., & Trushkin, S. A. 2010, MNRAS, 406, 307

Lallement, R. 2004, A&A, 422, 391

Lamers, H. J. G. L. M., Snow, T. P., & Lindholm, D. M. 1995, ApJ, 455, 269

Massey, P. & Thompson, A. B. 1991, AJ, 101, 1408

May, B. & Keel, W. C. 2008, in American Astronomical Society Meeting Abstracts, Vol. 211, American Astronomical Society Meeting Abstracts #211, 157.06

McCollough, M. L., Corrales, L., & Dunham, M. M. 2016, ApJL, 830, L36

McCollough, M. L., Smith, R. K., & Valencic, L. A. 2013, ApJ, 762, 2

Moffat, A. F. J., Corcoran, M. F., Stevens, I. R., et al. 2002, ApJ, 573, 191

Montmerle, T. & Townsley, L. K. 2012, Astronomische Nachrichten, 333, 355

Muno, M. P., Law, C., Clark, J. S., et al. 2006, ApJ, 650, 203

Nazé, Y., Chu, Y.-H., Guerrero, M. A., et al. 2002, AJ, 124, 3325

Pauldrach, A., Puls, J., & Kudritzki, R. P. 1986, A&A, 164, 86

Pittard, J. M. & Parkin, E. R. 2010, MNRAS, 403, 1657

Polcaro, V. F., Giovannelli, F., Manchanda, R. K., Norci, L., & Rossi, C. 1991, A&A, 252, 590

Preibisch, T., McCaughrean, M. J., Grosso, N., et al. 2005, ApJS, 160, 582

Rauw, G., Nazé, Y., Wright, N. J., et al. 2015, ApJS, 221, 1

Reipurth, B. & Schneider, N. 2008, Star Formation and Young Clusters in Cygnus, ed. B. Reipurth, 36

Schneider, N., Bontemps, S., Motte, F., et al. 2016, A&A, 591, A40

Schneider, N., Bontemps, S., Simon, R., et al. 2006, A&A, 458, 855

Schulte, D. H. 1956, ApJ, 124, 530

Smith, R. K., Brickhouse, N. S., Liedahl, D. A., & Raymond, J. C. 2001, ApJL, 556, L91

Smith, R. K. & Hughes, J. P. 2010, ApJ, 718, 583

Stevens, I. R. & Hartwell, J. M. 2003, MNRAS, 339, 280

Strickland, D. K. & Stevens, I. R. 1998, MNRAS, 297, 747

Townsley, L. K., Broos, P. S., Chu, Y.-H., et al. 2003, in Revista Mexicana de Astronomia y Astrofisica, vol. 27, Vol. 15, Revista Mexicana de Astronomia y Astrofisica Conference Series, ed. J. Arthur & W. J. Henney, 190–193

Townsley, L. K., Broos, P. S., Chu, Y.-H., et al. 2011a, ApJS, 194, 15

Townsley, L. K., Broos, P. S., Chu, Y.-H., et al. 2011b, ApJS, 194, 16

Uyaniker, B., Fürst, E., Reich, W., Aschenbach, B., & Wielebinski, R. 2001, A&A, 371, 675

Vink, J. S., de Koter, A., & Lamers, H. J. G. L. M. 2001, A&A, 369, 574

Vink, J. S., Drew, J. E., Steeghs, D., et al. 2008, MNRAS, 387, 308

Weaver, R., McCray, R., Castor, J., Shapiro, P., & Moore, R. 1977, ApJ, 218, 377

White, R. L. & Chen, W. 1995, in IAU Symposium, Vol. 163, Wolf-Rayet Stars: Binaries; Colliding Winds; Evolution, ed. K. A. van der Hucht & P. M. Williams, 438

Wilms, J., Allen, A., & McCray, R. 2000, ApJ, 542, 914

Wise, M. W. & Sarazin, C. L. 1989, ApJ, 345, 384

Wright, N. J. & Drake, J. J. 2009, ApJS, 184, 84

Wright, N. J., Drake, J. J., Drew, J. E., et al. 2012, ApJL, 746, L21

Wright, N. J., Drake, J. J., Guarcello, M. G., et al. 2014a, ArXiv e-prints

Wright, N. J., Drake, J. J., Guarcello, M. G., Kashyap, V. L., & Zezas, A. 2015a, ArXiv e-prints

Wright, N. J., Drew, J. E., & Mohr-Smith, M. 2015b, MNRAS, 449, 741

Wright, N. J., Drew, J. E., & Mohr-Smith, M. 2015c, VizieR Online Data Catalog, 744, 90741

Wright, N. J., Parker, R. J., Goodwin, S. P., & Drake, J. J. 2014b, MNRAS, 438, 639

Yusef-Zadeh, F., Law, C., Wardle, M., et al. 2002, ApJ, 570, 665

APPENDIX

Diffuse X-ray emission of individual ObsID maps:

In Figures 18 to 21, we show the individual diffuse X-ray maps (flux and hardness ratio) for the entire set of observations performed for the Cygnus OB2 Chandra ACIS-I survey. Each map is 17 sq.arcmin. The first and third columns show flux in the 0.5-7.0 keV energy band. Using the thermal model of the X-ray spectral fit (see section 6), we have computed the validated photon keV-to-erg conversion in the [0.5-7.0] keV band to be 1 ph = 4.18×10^{-9} ergs, which allows for conversion of diffuse maps of observed photon counts to absorbed flux. The X-ray flux is in CGS photon units. Hardness ratio images are displayed in the second and fourth columns, respectively. They were computed as the ratio (S-H)/(S+H). True diffuse emission was only considered whenever $HR > -0.1$, corresponding to the colors green, yellow and red in the HR maps (see section 4 for details). Intensities are illustrated on a single color scale of log(L_x)=[-17.08,-16.63] and HR=[-0.3,0.5] to facilitate comparison between flux and HR maps, respectively.

The filled and open symbols all over the maps refer to massive stars with and without intrinsic X-ray emission, respectively. Stars correspond to evolved objects, while circles represent MS stars. X symbols refer to massive OB type stellar candidates from Wright et al. (2015c).

NOTE: DUE TO LARGE NUMBER OF FIGURES IN THE APPENDIX AND DISK USE LIMITS IN ASTRO-PH, MAP WILL BE ONLY AVAILABLE ON THE ApJSS (CYGNUS OB2 SPECIAL ISSUE) VOLUME.